DUAL PURPOSE COOLING PLATES FOR THERMAL MANAGEMENT OF LI-ION BATTERIES DURING NORMAL OPERATION AND THERMAL RUNAWAY

THESIS

Presented In Partial Fulfillment of the Requirements for the Degree Master of Science in the Graduate Faculty of The University of Akron

By

Abdul Haq Mohammed
May, 2018

DUAL PURPOSE COOLING PLATES FOR THERMAL MANAGEMENT OF LI-ION BATTERIES DURING NORMAL OPERATION AND THERMAL RUNAWAY

Abdul Haq Mohammed

THESIS

Approved:	Accepted:
Advisor Dr. Siamak Farhad	Dean, College of Engineering Dr. Donald P. Visco Jr.
Co-Advisor Dr. Gopal Nadkarni	Executive Dean, Graduate School Dr. Chand K. Midha
Faculty Committee Member Dr. Alper Buldum	
Faculty Committee Member Dr. Reza Madad	
Chair, Department of Mechanical Engineering Dr. Sergio Felicelli	Date

ABSTRACT

Battery Thermal Management Systems are necessary for the overall efficiency and life cycle of vehicle as well safety of passengers and vehicle, as elevated operating temperatures have adverse effect on the efficiency, life cycle and safety of the Li-ion battery packs. The operating temperature prescribed by many studies for improved performance and better life cycle of Li-ion batteries is around 25°C. In some worst case scenarios, high operating temperature may lead to thermal runaway in the battery, causing immense amount of heat generation, even leading to an explosion. To avoid all these dangerous events, battery thermal management is utilized to regulate the temperature of the battery pack.

In this thesis, a novel battery thermal management system based on liquid cooling principle is proposed. The system involves dual purpose cooling plate for prismatic Li-ion batteries, which can maintain the temperature under normal conditions as well as mitigate the heat generated during thermal runaway. An experiment was performed on the prismatic Li-ion battery to measure the heat generation trends. The battery was discharged at 5C to replicate aggressive conditions. The data for maximum heat flux generated in the Li-ion battery was obtained. An estimated amount of heat generated during thermal runaway was calculated. A conjugate heat transfer method was used to simulate the cooling plates for normal operation and thermal runaway. The plates were simulated with two flow rates for normal operation and three flow rates for thermal runaway. Three different designs of cooling plates were compared on the basis of surface temperature, pressure drop and flow

rate. The final design was selected based on the comparison with the rest of the cooling plates. The selected cooling plate can:

- Maintain the temperature of battery below 25°C during normal operation.
- Dissipate the maximum possible heat generated during thermal runaway and bring the temperature to less than 80°C.
- Maintain least possible pressure drop in both conditions.

A stress and modal analysis was performed on the final cooling plate to analyze the structural integrity of the design. The selected cooling plate porotype was manufactured.

DEDICATION

This thesis is dedicated to

My father, mother, sister, brothers, and extended family back home for their continuous support, love and encouragement throughout my career and life.

All my teachers for molding and shaping my career and helping me reach this position in my life.

All my seniors and friends for motivating and supporting me through my journey and helping me in making the right decisions.

ACKNOWLEDGEMENTS

I would like to express my sincere gratitude to Dr. Siamak Farhad, my advisor and mentor for believing in me, who gave the motivation for this research and for his continuous guidance in technical issues with advices for life. I also owe my deepest gratitude to Dr. Gopal Nadkarni, my co-advisor and mentor for motivating me to pursue research, for giving me invaluable advices and guidance for my work and life. I would also like to appreciate the financial support from Ohio Federal Research Network (OFRN) and The University of Akron.

I would also like to express gratitude to my fellow colleagues at the Advance Energy and Sensor Lab here at The University of Akron for their immeasurable advice and help during my research. I would also thank Mr. Evan Foreman and his team for conducting the experiments. I also thank all my friends at The University of Akron for supporting me in my master's journey and making The University of Akron, a home away from home for me. I would also like to appreciate the support during my work from the design teams such as the Zips Racing, the Zips Electric Racing, the Finite Element Analysis Team and the Corrosion Design Team.

Lastly, I would like to thank Arsenal FC for teaching me how to sustain failure and bounce back and gratitude to all the individuals who have influenced my life knowingly and unknowingly.

TABLE OF CONTENTS

LIST OF TABLES

LIST OF FIGURES

Figure Page

LIST OF SYMBOLS

Symbol	Entity
$\rho\rho$	Density
C	C-rate
CC_{pp}	Heat Capacity at constant pressure
TT	Temperature
tt	Time
QQ	Heat Energy
pp	Pressure
$LL_{eeeeeeeeee}$	Entrance Length
$pp_{eeeeeeeeee}$	Entrance Pressure
$\mu\mu$	Dynamic Viscosity
kk	Thermal Conductivity
u	Velocity
Re	Reynolds Number
l	Length of the inlet
w	width of the inlet
DD_h	Hydraulic Diameter
Δpp	Pressure Drop
ff_{DD}	Friction Factor
LL	Length of Channel

CHAPTER 1

INTRODUCTION

1.1 Background

With the development of electric vehicles, the governments and automotive industry around the world are working towards making electric vehicles the primary mode of transportation to reach the goal of clean and green environment. The current research is now focused on developing safe, inexpensive and more reliable electric vehicles. Another area of research is the aviation industry where small electric aircraft have already have garnered the interest of hobbyists and start-ups. Aviation giants like Boeing and Airbus etc. across the globe are the supporting the new start-ups that are venturing to develop hybrid electric aircraft. Scientists and engineers are developing batteries which have more power capacity and are cheaper than the current batteries present in the market. As the power in the batteries increases, the vehicle's range increases.

As these vehicles and aircraft require an immense amount of power to operate, the Li-ion batteries are generally coupled in series or parallel to deliver the required amount of power. The performance of these vehicles and aircraft is primarily dependent on the Li-ion batteries, hence Li-ion batteries have become a crucial component of research and development. Li-ion batteries generate heat during their operation and are susceptible to degradation, if the operating temperatures exceed the manufacturer specified conditions.

In the hybrid electric vehicles and aircraft, Li-ion batteries are stacked in an array to form a battery pack. The Li-ion batteries release around 8-10% of their total energy as heat energy and as the number of the batteries increases inside the battery pack, the amount of heat generated from the battery pack also increases. Elevated temperatures can affect adversely on the efficiency, durability, power, and safety of the batteries. For this very reason, thermal management is vital for the battery packs to maintain and control the operating temperatures around the batteries. The primary aim of the battery thermal management system is to dissipate the heat generated in the battery pack. A battery thermal management system can incorporate various techniques such as air cooling, liquid cooling, phase-change materials PCM, or heat pipes or even a combination of the two or more of above techniques. However, the task of removal of heat generated from the battery pack is not simple. An efficient battery thermal management system not only involves cooling/heating techniques but also various monitoring systems to analyze the health of the batteries.

In this chapter, a brief introduction of heat generation in the Li-ion battery is explained and the vitality of the battery thermal management systems is discussed. A review of the current technologies available for battery thermal management is studied to recognize the gaps and scope for the work of this thesis.

1.2 Li-Ion Battery

With the advent of 21st century, the Li-ion batteries have become an important source of power with applications ranging from communication to transportation. Sony released the first battery in 1991 and over the years, Li-ion batteries replaced every other rechargeable power source due to their high power density and long life cycles But due to

the complexities, hybrid electric vehicles required batteries with more power and better life cycles The current research is focused on increasing the energy and power density of the Li-ion batteries while providing longevity, improved safety, and cost-effectiveness.

A typical Li-ion battery has a cathode (positive charges electrode), an anode (negative charge electrode), a separator and an electrolyte packed inside a metal casing. The electrons move from anode to cathode through the electrolyte. The anode oxidizes, releases electrons to the electrolyte and cathode accepts the electrons from the electrolyte. The Li-ion batteries are rechargeable which correlates that the electrochemical reactions occurring are reversible. In batteries, the chemical energy is converted into electrical energy and according to the second law of thermodynamics, any conversion between two forms of energy (chemical energy to electrical energy) occurs with an energy (heat) loss. Heat is produced in the batteries due to three fundamental process such as activation of interfacial kinetics, species transport phenomenon and joule heating from the movement of charged particles [1]. The heat generated in the small batteries is negligible but as the size of the battery increases, there is a significant increase in the amount of heat energy generated.

The failure mechanisms of Li-ion battery are thermal abuse, physical damage, short circuit and charge and discharge failures which generally lead to internal short-circuit in the battery. Internal short-circuit is one of the catastrophic failures to prevent. During internal short-circuit current passes internally through the cell causing many scenarios like decomposition of electrodes and separator. This also leads to excessive heat generation, the release of toxic, explosive and carcinogenic gases and in some unfortunate cases, causing an explosion [2].

1.3 Battery Thermal Management

Li-ion batteries generate heat during the conversion process of chemical energy to electrical energy. Another source of heat generation in Li-ion batteries is Joule heating effect, where the energy of an electric current is converted into heat as it flows through a resistance. The heat energy generated during the charging and discharging and if the heat generated is not removed from the system, it gets accumulated causing an increase in the temperature of the battery pack. As the operating temperature increases, the rate of degradation in all the components of the Li-ion battery increases [3]. Khateeb et al. studied the effect of operating temperature on the performance and life cycle of the Li-ion batteries and concluded that the electrochemical process, charge acceptance rate, power, and energy density, life cycle and cost are governed by the operating temperature [4]. T.M. Bandhauer et al. discussed various thermal issues of Li-ion batteries and the effect of operating conditions on recoverable power and capacity of the battery and concluded that the LIB show a reduction in recoverable power and capacity if the batteries are stored at ~50°C and the capacity of Li-ion battery reduces if the cycling temperature is below -10°C [1]. The optimum operating temperature for Li-ion batteries as suggested by various studies is 25-40 °C for maximum performance and better life [5] [2].

Another cause of concern for the safety of the Li-ion batteries is batteries undergoing thermal runaway. Thermal runaway is a phenomenon that occurs in the battery at elevated surrounding temperatures, initiating series of exothermic side reactions[6] [7] with a rapid increase in the internal temperature in a short span of time. This leads to a much-accelerated rate of reactions inside the battery casing electrodes to decompose, generating excessive heat energy in the process. If the heat generated is not dissipated

effectively, it will lead to an increase in the overall temperature of the battery pack. During thermal runaway, the temperature inside the battery can rise to 870°C and the temperature difference (hottest region vs coldest region) within the battery can reach 520°C [8]. The process of thermal runaway occurs in less than 10 seconds [9] and the amount of heat generated is in the magnitude of 10^7 W/m^3 [10]. During the process, excessive amount of highly explosive, hazardous and carcinogenic gases are released, which can lead to ignition in adjacent cells [11]. This is a catastrophic effect on battery pack as one cell undergoing thermal runaway can cause a chain reaction on rest of the cells in the battery pack, thus initiating thermal runaway in the adjacent cells which can lead to an explosion.

An ideal battery thermal management system should maintain the battery pack's temperature in the optimal range and enhance the lifetime of the battery pack without compromising on the safety of the entire system. It should be able to maintain the minimum temperature difference between different cells in the battery pack. The battery thermal management system should also be compact, lightweight, and cost-effective without sacrificing the functionality of the system. The BTMS should perform cooling, heating, ventilation, or insulation operations depending on the operating requirement.

A traditional BTMS comprises of cooling, heating, and insulation components along with a control unit to monitor the status of each cell. The amount of heat generated determines the size and intensity of the BTMS. Khan et al. have compiled the current standards and literature available to design an ultimate battery thermal management system and provided recommendations on enhancing the thermal performance of the batteries and improving the lifetime, reliability and efficiency of the BTMS [12].

Jeremy Neubauer and Eric Woods studied the effects of real-world climatic conditions on the batteries of electric vehicles. The study concluded that hot climates increase the battery wear leading to a reduction in the efficiency of the vehicle whereas cold climatic conditions have minimal effect on the utility of the vehicle. The cold climates cause difficulty in cabin heating and hot climates cause high peak on-road temperatures[13].

1.4 Techniques of Battery Thermal Management

Over the years, researchers developed different techniques to dissipate heat from the battery pack and maintain the temperatures within an optimal range. Air cooling, liquid cooling, phase change material (PCM) and heat pipes are some of the techniques. The focus has always been to attain maximum efficiency and cost-effectiveness without affecting the safety of the system. Depending upon the operating requirements, any of the above techniques or a combination can be utilized for cooling and heating the battery pack.

1.4.1 Air Cooling Method

Air cooling system utilizes air as the medium of heat transfer. Air cooling is of two types, natural air cooling which implies allowing air its natural speed and forced air cooling where the air is forced into the battery pack by a blower. The air can be from the atmosphere or HVAC system of the vehicle. This is the cheapest method available but the temperature difference between air and cell can be greater than 15°C, which is a limitation of this method [12].

The effectiveness of the air cooling depends on the arrangement of the battery cells. Wang et al. studied different cell arrangements for cylindrical battery cells and concluded

that the cubic arrangement is the best option. The cooling ability of air-cooled BTMS is influenced by speed, length, and cross-sectional area of air flow path. The placement of the fan on top significantly increase the effectiveness of the air cooling system as generally maximum heat in the battery is generated on the upper region [14]. Chen et al. performed a comparative study on four different configurations of cooling methods namely air cooling, fin cooling, indirect liquid cooling, and direct liquid cooling. The study concluded that the air cooling draws maximum power and indirect cooling has the least temperature gradient for increasing mass flow rate [15].

Fan He and Lin Ma proposed an active temperature control and reciprocating cooling air flow method for cylindrical cells. They developed a reduced order model of the thermal behavior of the battery studied the core and surface temperature of the cell. The study also concluded that the active control and reciprocating flow can reduce the temperature gradient significantly and observed a reduction in the quantity of air required for cooling [16]. Xu et al. designed a U-type duct for forced air cooling with results indicating the improvements in the heat dissipation by changing the longitudinal battery pack to horizontal battery pack. They also concluded that improper heat dissipation reduces the SOC, charge and discharge rate of the battery [17]. Giuliano et al. conducted an experiment to evaluate ambient air as the fluid for BTMS for 50 Ah Lithium Titanate cells and dissipate heat through natural convection. The design maintained the temperature of the battery pack 10°C above ambient temperature (22°C) [18]. Mohammadian and Zhang proposed a design for a novel pin-fin heat sink and concluded that pin-fin heat sinks have improved efficiency than conventional heat sinks. The increase in inlet velocity decreases

the maximum temperature of the battery and increase in the inlet air temperature increases the maximum temperature of the battery [19].

1.4.2 Phase Change Materials

Phase change materials (PCM) is a passive thermal management system. PCM eliminates the requirement of cooling equipment and increases the available power for utilization by the vehicle. The PCM can be incorporated in the battery pack and they act as heat sinks. The PCM are materials with the high latent heat of fusion which enables them to absorb large quantities of heat. The PCM starts to melt when the battery cell's temperature exceeds the melting point of PCM preventing a steep rise in the temperature of battery pack [20]. The PCM can be effective in cold climates as heat absorbed by PCM is stored as latent heat and released during normal temperature, thus maintaining a higher temperature compared to the surroundings [21]. Wang et al. proposed paraffin and paraffin/aluminum foam composite as PCM and proved that composite PCM has more heat absorption compared to pure paraffin. The addition of aluminum foam increased the melting rate of PCM. The battery showed increased temperature during discharging in the absence of aluminum foam and paraffin in the PCM [22].

1.4.3 Heat Pipes

Heat pipes are metallic structures placed in between cooling fins and batteries and utilizes capillary structure to drive the liquid to the evaporator. The battery (heat source) is on the evaporating side of heat pipe and the cooling fins (heat sinks) are on condensing side [23]. Q. Wang et al. conducted experiment on the heating and cooling of batteries with heat pipes. The study concluded that the heat pipes successfully maintained the temperature

below 40°C and could heat the batteries right after been exposed to -15°C for 14 hours [24]. Mao-Sung Wu et al. proposed aluminum fins with heat pipes and concluded that a temperature difference of 20°C was noticed at the end of discharge. The heat pipe in direct contact cannot efficiently dissipate the heat but the heat pipe with aluminum fins exhibited better heat dissipation and the temperature difference was negligible [25].

Pulsating heat pipes are similar to heat pipes with a contrast that the liquid flow is not driven by capillary structure instead liquid is induced with vapor bubbles rising from the evaporator and settling in the condenser. G. Burban et al. studied four fluid for different inclinations and achieved the same thermal resistance of 0.13 K/W [26].

1.4.4 Liquid Cooling Method

The liquid cooling method involves a liquid as the medium for heat transfer. There are two types of liquid cooling methods, direct contact, and indirect cooling. In direct cooling, the batteries are submerged in mineral oil and for indirect cooling, water/glycol is passed through cooling plates/fins. A liquid cooling system generally consists of a pump, a radiator, and cooling mechanism (plates or fins). Jarrett and Kim studied the effects of operating conditions and produced an optimum design of cooling plate by comparing four different configurations of flow pattern. They optimized the design for temperature uniformity for the boundary conditions but the pressure drop was not sensitive to any of the boundary conditions [27]. They also proposed another design study with increased channel width and performed optimization using CFD analysis. This study concluded that pressure drop and average temperature decreases with increase in the width of the channel. The study also stated, "The design for temperature uniformity has a narrow inlet channel

widening towards the outlet; this balances the effects of coolant velocity, heat transfer area, and fluid-solid temperature gradient to equalize the heat transfer from all areas of the plate" [28]. L.W. Jin et al. designed a liquid cold plate with oblique fins with ultra-thin minichannels. The oblique fin model maintained lower temperatures compared to the straight channels. By increasing the flow rate, the cold plate dissipated increased heat loads and maintained the temperature below 50°C [29].

Dai Haifeng et al. proposed four cooling plates with different cooling channels (S-type and linear type) and compared those using CFD simulations. As the area of contact is more in S-type channels, they absorb more heat and maintain better temperature distribution compared to linear type channel [30]. M. M. Rahman et al. developed a cold plate heat exchanger with the flow channel. The results showed that the outlet temperature decreased with the increase in mass flow rate of the water [31].

Jian Xu et al. proposed a minichannel design to prevent thermal runaway. They performed a nail penetration test and caused thermal runaway in the battery. The minichannel could not mitigate thermal runaway at the cell level with a flow rate of 10 L/min but it dissipated the heat, preventing thermal runaway propagation to other cells. It also maintained the temperature around 60°C [10] . Chuanjin Lan et al. studied four configurations of minichannels and performed a parametric study on them. With the same flow rate, the cooling abilities increased significantly by increasing the number of minichannels. The minichannels were able to maintain a temperature difference of 1°C for 1.5C discharge rate and 1.26°C for 2C discharge rate [23].

1.5 Scope of Research

Battery thermal management is a complex subject as the safety and efficiency of the electric vehicles along with passengers is at stake. Li-ion batteries have gained importance due to their high power density and longer life cycles. Li-ion batteries generate heat during the conversion process of chemical energy to electrical energy. Another source of heat generation in Li-ion batteries is Joule heating effect, where the energy of an electric current is converted into heat as it flows through a resistance. The heat generated can inversely affect the durability and efficiency of the battery, hence heat dissipation mechanisms are a necessity for batteries and battery packs. The optimum operating temperature for Li-ion batteries as specified by many studies and manufacturers is between 20°C – 40°C.

Different techniques of BTMS can be utilized to perform heating and cooling operations depending upon the requirement of the battery pack. The passive cooling methods are effective in heat dissipation, but they maintain the temperatures around the higher scale of operating temperature. The active cooling methods require cooling equipment and maintain the temperature around ~25°C.

Thermal runaway is a deleterious phenomenon causing Li-ion batteries to decompose within few seconds releasing a huge amount of heat with toxic gases and may even cause an explosion. It is difficult to prevent thermal runaway in a battery, but it can be stopped from spreading across the battery pack by containing the heat generated during this phenomenon.

Most of the studies and research focused on heat dissipation during normal operation of the battery but only one design could dissipate heat during and after thermal runaway [10]. A majority of the current battery thermal management systems are focused on cylindrical batteries. The particular area of battery thermal management systems for large prismatic Li-ion batteries was not much explored due to the complexities and safety hazards related to thermal runaway.

1.6 Objective of Thesis

This work contributes to the area of liquid cooling methods for thermal management of Li-ion batteries. The goal is to develop of a novel design of dual-purpose cooling plate for a large prismatic Li-ion battery pack. The cooling plate should be able to maintain the surface temperature of battery around manufacturer's specified operating conditions as well as dissipate the heat generated in the battery during thermal runaway.

CHAPTER 2

EXPERIMENT AND MODELLING

2.1 Thermal Model of Li-ion Battery

As Li-ion batteries generate heat during operation, it is necessary to identify the trends and obtain the amount of local heat flux generated at different states of charge (SOCs). For this reason, an experiment was designed and conducted on large prismatic Li-ion battery. The objective of this experiment was to determine the heat generated in the battery at 5C. C-rate is rate of charge and discharge of the battery and it's denoted by "C". It implies that that the battery at 1C rate will discharge completely in one hour and the also means the battery of 10 Ah will discharge 10 amps of current in one hour. It is noted that 5C is the maximum continuous discharge rate of the LIB studied as suggested by the manufacturer.

2.1.1 Heat Flux Experiment

A prismatic Li-ion battery with graphite anode and $LiFePO_4$ cathode was equipped with seven heat flux sensors. One thermocouple is attached to each heat flux sensor. The battery was cycled using BCS-815 Biologic battery cycler. The location of the sensors was chosen to accommodate maximum area and crucial spots such as battery terminals. The sensors were placed as shown in Figure 2.

.

To activate the battery, it was charged and discharged 10 times at 1C. In order to simulate aggressive thermal conditions, a higher rate of discharge (5C) was utilized, i.e. 90 amps The experiment was monitored and controlled in a real time situation [32], [33] with the help of battery cycler.

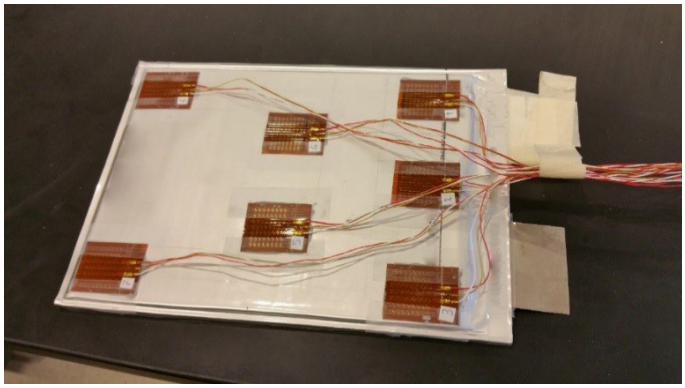

Fig 1. Sensor placement on the front side of commercial prismatic Li-ion Battery.

Table 1. Thermal properties of heat flux sensors.

Thermal Resistance	0.004 °C/(W/m^2)
Thermal Capacitance	1000 W.s / m^2. °C
Response Time	0.7 seconds

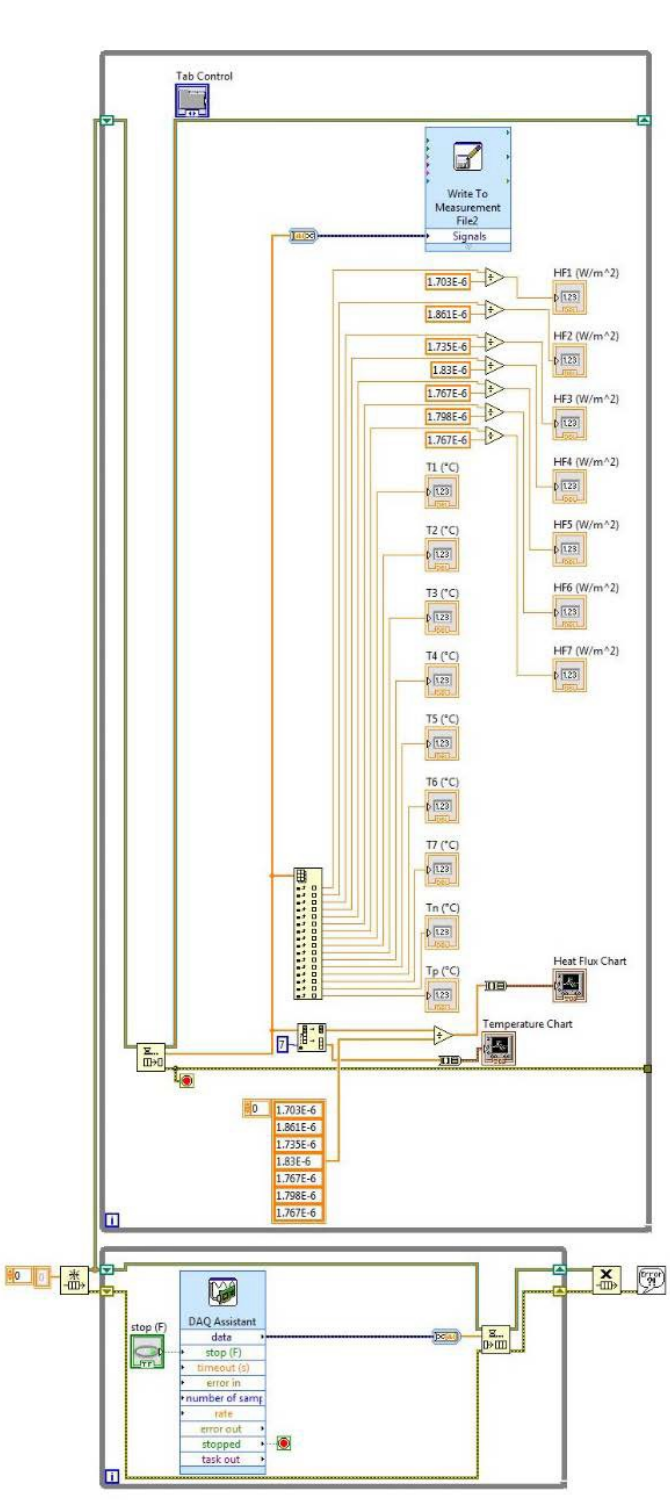

Fig. 2. LabVIEW VI

A custom LabVIEW VI was developed to collect data from heat flux sensors and thermocouples during the operation of battery at 5C for discharge and 1C for charge. The same experiment was performed on the other side of the same battery. The heat flux and temperature data were collected at the rate of 1Hz for 720 seconds (from the battery SOC of 0 to 100%). As the test begins, the LabVIEW displayed the data for temperature and heat flux and stored the data in a text file. After the completion of the test, the values of local heat fluxes from SOC of 0 to 100% at every 0.14% change of SOC are available and were used for designing cooling plates. We observed from the experimental results that there is a SOC at which the local heat generation in the battery is the highest [34].

Since the cooling plates should control the battery temperature even at the highest rate of heat generation, we found the highest heat flux from the recorded data and performed the cooling plate design based on the rate of heat generation. Table 1 shows the value of maximum heat generation recorded by each heat flux sensor. The volumetric heat generation (W/m^3) was calculated from the recorded heat flux (W/m^2) by dividing it with half of the battery thickness. The heat flux sensors are very thin and their thermal impedance is negligible compared to the thermal impedance of the battery.

Table 2.Maximum heat generation in the battery based on the seven sensors

Sensor/Zone	Maximum Heat Generation (W/m^3)
1	212,705
2	277,014
3	286,491
4	199,166
5	209,750
6	152,305
7	195,186

From Table 1 and Fig.1, it is evident that the top region of the battery (near terminals) generates much more heat flux compared to the bottom and mid region. To simulate the worst case-scenario, the above heat generation was applied as constant heat source in the simulation. The overall error of the experimental results including the errors of sensor and data acquisition system is less than 8%. In the experiment we assumed that the effect of radiation heat transfer is negligible and all heat generated in the battery is dissipated by convection. It was also assumed that the heat flux measured by each sensor represents the average heat flux in the region of the battery that the sensor is mounted. The thermal impedance of the heat flux sensor is also neglected [35].

2.1.2 Thermal Model of Li-ion battery

After collecting the data and calculation the maximum heat generated in all the seven zones of the battery, a computational model was created in COMSOL, a commercial CAE software to simulate the worst-case scenario. The heat flux equation obtained were used as input to determine the temperature distribution along the surface of the battery. As the experiment was conducted on each side separately, only half of the battery was simulated for accurate results. A time dependent study was performed for 720 seconds. The results reported the maximum temperatures at the top of the battery near terminals. To simulate the worst case scenario, the maximum heat flux generated were used as input. The maximum temperature was 79.4°C (fig.3), which significantly above the specified operating temperature of the battery (i.e.) around 25°C.

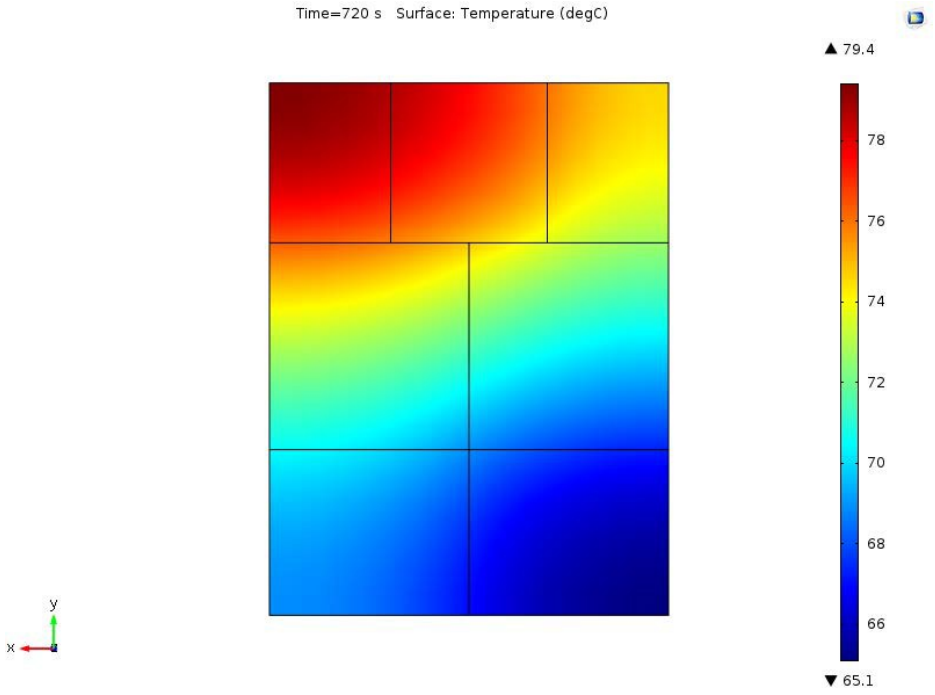

Fig. 3. Battery maximum surface temperature – Worst case scenario

2.1.3 Thermal Runaway Model of Li-ion Battery

A model of Li-ion battery undergoing thermal runaway was created to understand the heat generation and simulate the design of cooling plate for thermal runaway. The amount of energy stored in the battery was calculated and the time a battery undergoes thermal runaway is approximately 10 seconds. This phenomenon drains the total battery at an accelerated speed releasing heat energy as the materials inside the battery decompose due to chemical reaction with each other. An estimate on amount of energy released during the process was calculated.

Capacity of the prismatic Li-ion battery:

$$20\ AAh, 3.3\ VV$$

(1)

Volume of the battery under study:

$$160 \times 225 \times 7 \times 10^{-9}\ mm^3$$

(2)

Total Energy Stored in battery:

$$20\ AAh\ \times 3.3\ VV\ = 66\ WWh$$

(3)

$$66\frac{JJ}{ss} \times 3600\ ss = 237600\ JJ$$

(4)

$$\frac{237600\,JJ}{160 \times 225 \times 7 \times 10^{-9}\,mm^3} = 0.943 \times 10^9 \frac{JJ}{mm^3}$$

(5)

For 10 seconds:

$$\frac{0.943 \times 10^9 \frac{JJ}{mm^3}}{10\,ss} = 94.3 \times 10^{6\text{-}} \frac{WW}{mm^3}$$

(6)

The amount of energy released during 10 seconds of thermal runaway is approximately 100 $\frac{MMMM}{mm^3}$. The surface temperature on the battery can reach to 1000°C depending upon the capacity of the battery and rate of reaction during thermal runaway.

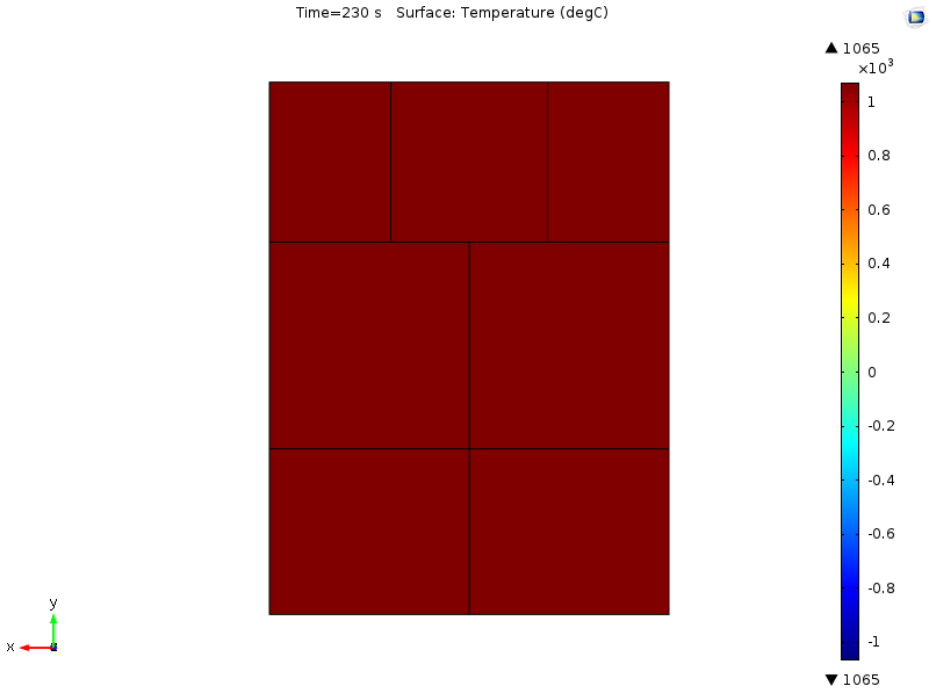

Fig. 4. Battery maximum surface temperature after thermal runaway

2.2 Simulation of Plate and Battery

2.2.1 Computational Model

The computational model consists of single cooling plate and battery cell. The actual dimensions of the plates are 225mm (height), 162mm (width) and 7mm (thickness) and the battery cell are 204mm (height), 153mm (width) and 7mm (thickness). The fluid flows inside the plate through the path described by geometry, performing the cooling action. The components are sectioned along the thickness to cut through half and simulation is performed on one section of cooling plate (i.e.) cooling action of half battery and half plate because of the symmetric conditions. For the computational model, the thickness of the plate and battery was reduced to 3.5mm. This was done to decrease the number of elements in the simulation to half, thus reducing the computation time drastically. For Normal Operation simulation, the battery is divided into seven sections as discussed above but instead of using average heat flux equations as input, the maximum heat flux was used to simulate the worst case scenario. The maximum heat flux generated in each zone is listed in Table 1. The flow rates used were 0.2 L/min and 0.3 L/min to simulate the Normal Operation.

For thermal runaway, the battery was considered as one part and heat source was applied using step functions. To simulate a real time scenario, the battery was initialized for 200 seconds with heat of 0.3 MW/m^3 and warmed up to 23°C. Then, as calculated above, a heat of 100 MW/m^3 was applied for 10 seconds to simulate the thermal runaway and then the heating was terminated. The coolant flow was also controlled by the step functions. The initial flow of 0.3 L/min was applied for 200 seconds, thus maintaining the temperate of battery around 23°C. As the thermal runaway was initiated, the flow rate was

increased to 20 L/min, 30 L/min and 40 L/min with the help of parametric sweep. The coolant was applied for next 30 seconds to allow for the removal of heat generated during thermal runaway. The expected result from this simulation is the ability of the cooling plate to maintain the temperature of the battery by dissipating the heat even after undergoing thermal runaway. The below fig. 5 shows the surface temperature of the battery without any cooling effect and the battery temperature increases to 1000°C during thermal runaway. From 0 to 200 seconds, the battery operates normally and the sudden rise in the temperature at 200 seconds is due to the initialization of thermal runaway.

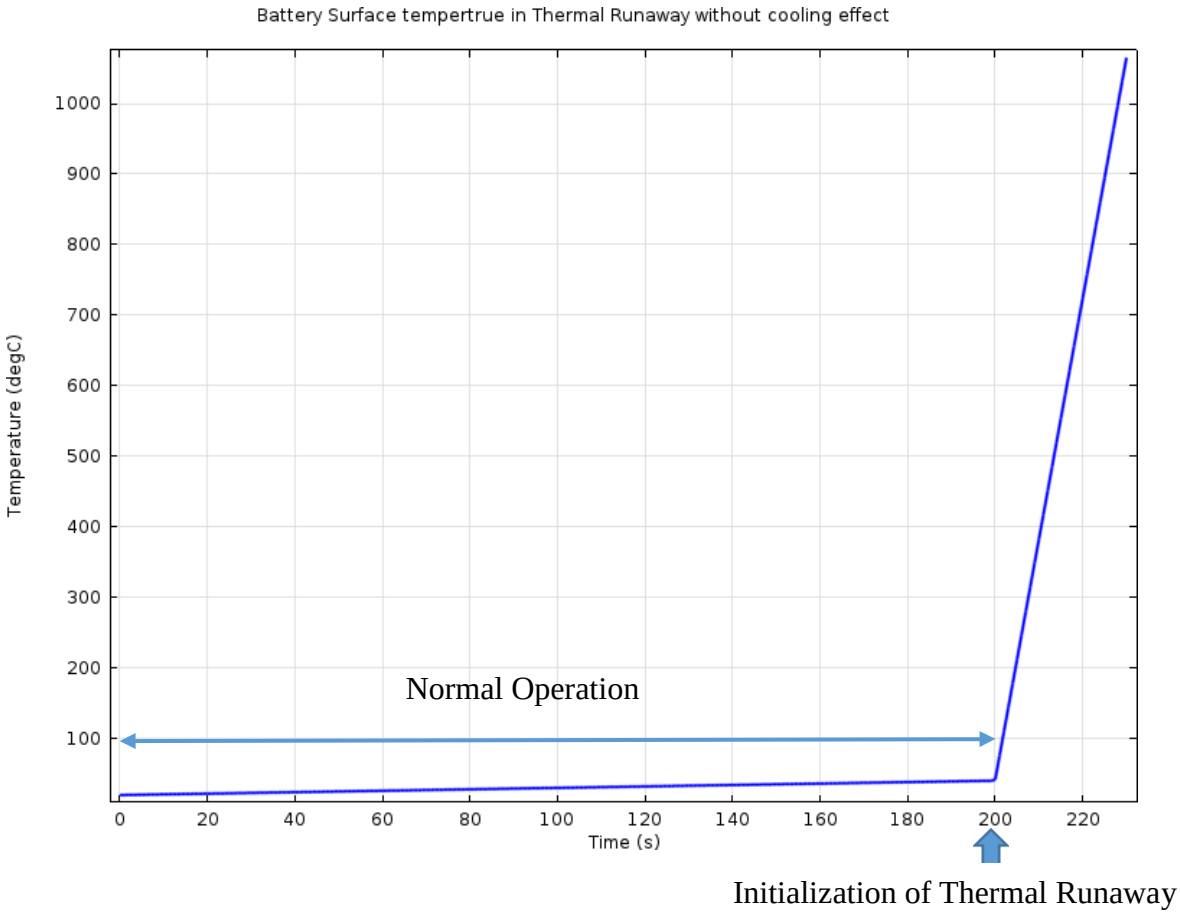

Fig. 5. Battery maximum surface temperature during thermal runaway without cooling plate.

Aluminum 6063 was selected as the material for the cooling plates due to its light weight, high strength to weight ratio and high thermal conductivity. The ultimate tensile strength of Aluminum 6063 is 260 MPa. The fluid was selected as water for high heat capacity and low viscosity. The thermal conductivity, density and heat capacity for the plate and coolant were assigned through the predefined library in the simulation. For the batteries the following properties were selected. A density of 2100 kg/m^3 and heat capacity of 1400 J/ (kg-K). The heat generation in the battery was calculated to be anisotropic in nature. The constituent components of the battery have different thermal conductivities and thicknesses. The thermal conductivity was calculated considering the direction of heat flow. The x and y directions had series conduction and z direction had parallel heat conduction. The calculated values were 1.68 W/ (m.K) for z direction and 26.9 W/ (m.K) for x and y direction.

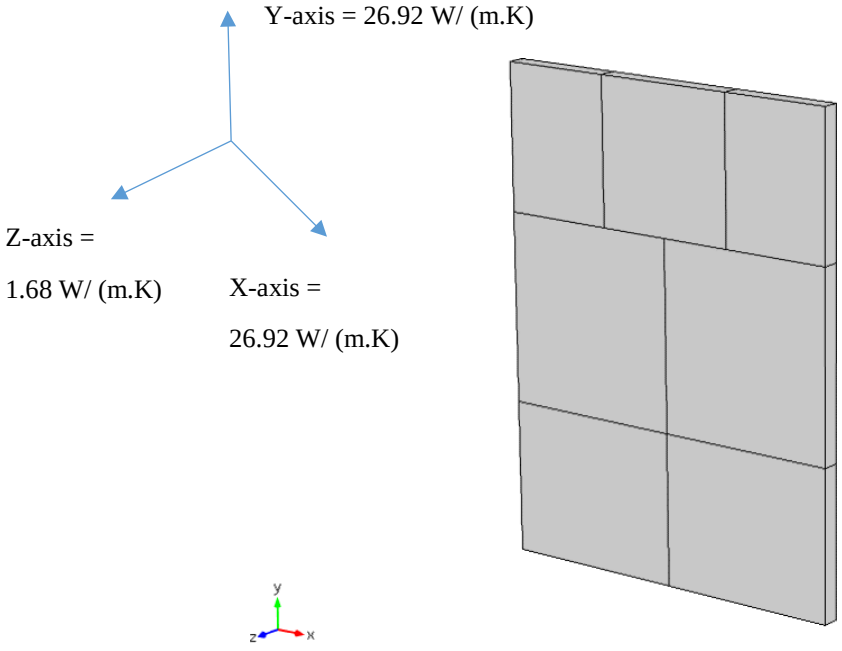

Fig. 6. Battery in the computational model and the direction of Thermal conductivities.

Table 3. Material properties used in all simulations.

Material Properties			
	Aluminum 6063	Water	Battery
Heat Capacity (Cp)	900 J/(kg.K)	4185 J/(kg.K)	1400 J/(kg.K)
Density (ρ)	2700 kg/m³	1000 kg/m³	2100 kg/m³
Thermal Conductivity (k)	201 W/(m.K)	0.6 W/(m.K)	1.68 W/ (m.K) in x & y direction. 26.92 W/(m.K) in z – direction
Dynamic Viscosity (μ)		0.00089 (Pa.s)	

COMSOL was utilized for the simulation. A Conjugate Heat Transfer Module which involves a combination of heat transfer and CFD for the problem was used. A non-isothermal flow condition was applied for the convective heat transfer. As the plate and cell are halved, symmetric boundary conditions were applied to identify symmetric conditions. The parametric sweep was applied at the inlet and the pressure was constrained to atmospheric pressure (i.e.) 0 Pa at the outlet. An optimum mesh was generated considering the intricacies of CFD and time dependent study for 1000 seconds for Normal Operation and 230 seconds for thermal runaway was performed. The optimal desired operating temperature for the battery was identified between 22°C – 25°C for normal operation. To achieve the desired conditions, the plate was simulated for increasing flow rates and the effect of cooling on the surface temperature of battery and pressure drop at outlet were studied.

Table 4. Boundary Conditions used in Normal Operation and Thermal Runaway simulation.

Boundary Conditions	
Entity	Location
Heat Source	Battery
Initial temperature for all bodies	20°C
Initial Water Temperature	20°C
Atmospheric Pressure (0 Pa)	Outlet
Laminar Inflow (Flow rate)	Inlet
Symmetry	Symmetric Plane

2.2.2 Governing Equations

Heat Transfer in cooling plate and battery:

$$\rho_{pp}C_{pp}\frac{\partial T}{\partial t} + \rho_{pp}C_{pp}\,\mathbf{u}\cdot\nabla T = \nabla\cdot(k\nabla T) + Q$$

(7)

Heat Transfer in water:

$$\rho_{pp}C_{pp}\frac{\partial T}{\partial t} + \rho_{pp}C_{pp}\,\mathbf{u}\cdot\nabla T = \nabla\cdot(k\nabla T) + Q + Q_{vvv} + Q_{pp}$$

(8)

Momentum balance equation for water flow:

$$\rho\rho\frac{\partial\partial\mathbf{u}}{\partial\partial tt} + \rho\rho(\mathbf{u}\cdot\nabla)\mathbf{u} = \nabla\cdot \text{ } \diamond pp\mathbf{I} + \mu\mu(\nabla\mathbf{u}+(\nabla\mathbf{u})^{\mathrm{T}}) - \frac{2}{3}\mu\mu(\nabla\cdot\mathbf{u})\mathbf{I}\diamond + \mathrm{F}$$

(9)

Mass balance equation for water:

$$\frac{\partial\partial\rho\rho}{\partial\partial tt} + \nabla(\rho\rho.\mathbf{u}) = 0$$

(10)

Inlet boundary condition for water:

$$\mathit{LL}_{\mathit{eeeeeeeeee}}\nabla_{\mathrm{t}}\cdot \diamond pp\mathbf{I} + \mu\mu(\nabla_{\mathrm{t}}\mathbf{u}+(\nabla_{\mathrm{t}}\mathbf{u})^{\mathrm{T}}) - \frac{2}{3}\mu\mu(\nabla\cdot\mathbf{u})\mathbf{I}\diamond = -pp_{\mathit{eeeeeeeeee}}\mathbf{n}$$

(11)

Outlet boundary condition for water:

$$\diamond pp\mathbf{I} + \mu\mu(\nabla_{\mathrm{t}}\mathbf{u}+(\nabla_{\mathrm{t}}\mathbf{u})^{\mathrm{T}}) - \frac{2}{3}\mu\mu(\nabla\cdot\mathbf{u})\mathbf{I}\diamond\mathbf{n} = -pp_0\mathbf{n}$$

(12)

Outlet and symmetry boundary conditions for heat transfer in water, cooling plate and battery:

$$-\mathbf{nn}\cdot(kk\nabla TT) = 0$$

(13)

The symmetry boundary condition for water flow in the cooling plate:

$$\mathbf{u} \cdot \mathbf{nn} = 0$$

$$\mathrm{K} - (\mathrm{K} \cdot \mathbf{nn})\mathbf{nn} = \mathbf{0}\mathbf{0}$$

$$\mathrm{K} = \mu(\nabla\mathbf{u}+(\nabla\mathbf{u})^{\mathrm{T}}) - \frac{2}{3}\mu(\nabla\cdot\mathbf{u})\mathbf{I}$$

(14)

2.2.3 Mesh Independence

A mesh independent solution is a solution that does not vary with increase or decrease in the size of mesh elements. For this simulation, three different mesh sizes were studied. A coarse mesh with 201338 elements. A normal mesh with 236792 elements and a fine mesh with 250381 elements. The normal mesh size was used in all the simulation. The solution was independent of the mesh size.

Table 5. Mesh Independence Analysis

Mesh size	Maximum Surface Temperature (°C)	Number of Elements
Coarse	21.9	201338
Used	21.9	236792
Fine	21.9	250381

CHAPTER 3

DUAL PURPOSE COOLING PLATES

In any design process, there are always constant modifications for improvement of the design. The idea was to design a cooling plate which can operate in normal conditions as well as during thermal runaway. The criterion for the selection of cooling plate was the ability to maintain the temperature of battery below 25°C during normal operations, dissipate the maximum possible heat generated during thermal runaway and maintain as low as possible pressure drop during both the conditions. All the three plates developed were simulated as discussed in the previous chapter.

3.1 Normal Operation

3.1.1 Normal Operation in Design 1

The first design was a plate with numerous pins arranged in array. The inlet was 30 mm x 25 mm and the outlet 50 mm x 20 mm. The arrangement of the pins was set in way to disperse the fluid thoroughly inside the plate. The first design can be seen in Fig. 7. The size of the pin was selected to be 1 mm to have enough strength to withstand the pressure from fluid flow while not completely restricting the motion of fluid. During normal operation, the Design 1 was able to maintain the surface temperature of the battery below 23°C for both the flow rates of 0.2 L/min and 0.3 L/min, which is below the manufacturer specified operating temperature.

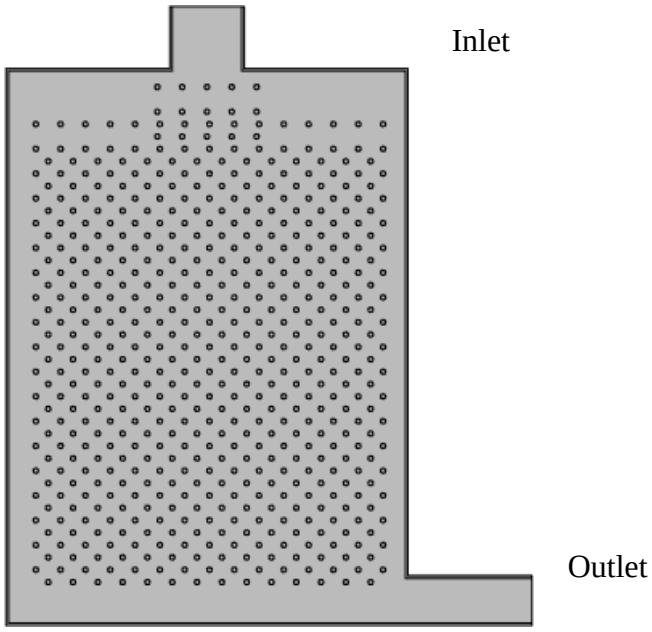

Fig. 7. Design 1 – sectioned front view.

The surface temperature for Design 1 with 0.2 L/min and 0.3 L/min can be seen below. The maximum temperature for 0.2 L/min was 22.7°C and for 0.3 L/min was 22°C.

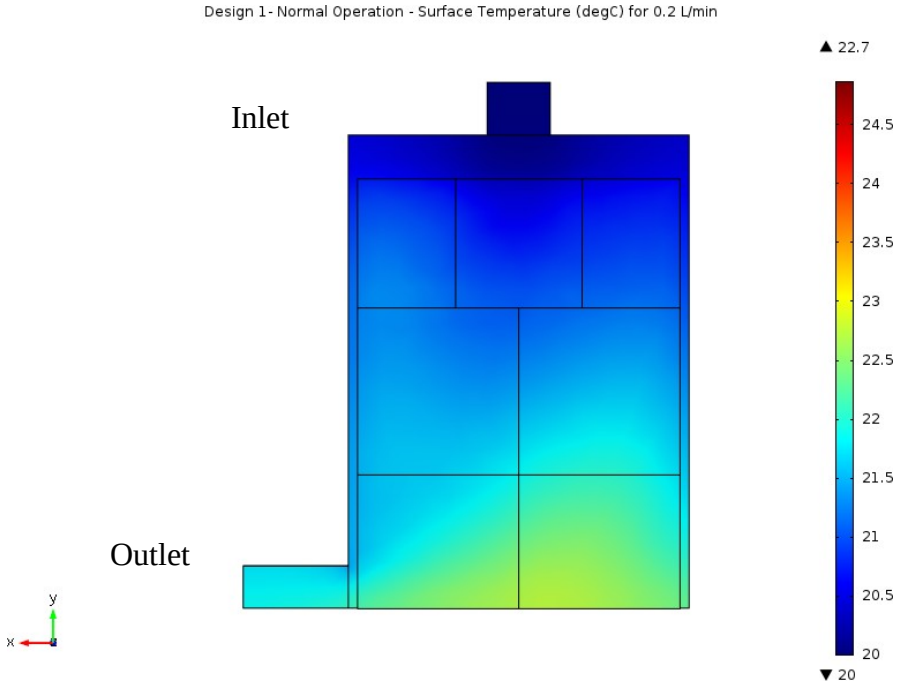

Fig. 8 (a). Design 1- Normal Operation - Surface Temperature (°C) for 0.2 L/min

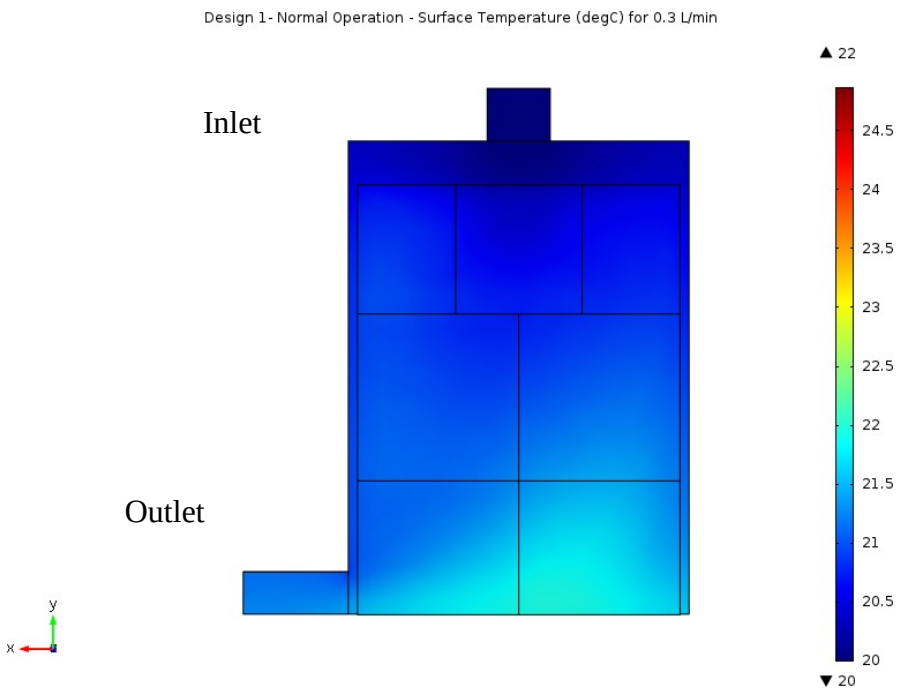

Fig. 8 (b). Design 1- Normal Operation - Surface Temperature (°C) for 0.3 L/min

The pressure distribution for Design 1 with 0.2 L/min and 0.3 L/min can be seen below. The pressure drop for 0.2 L/min was 53.9 Pa and for 0.3 L/min was 82.4 Pa.

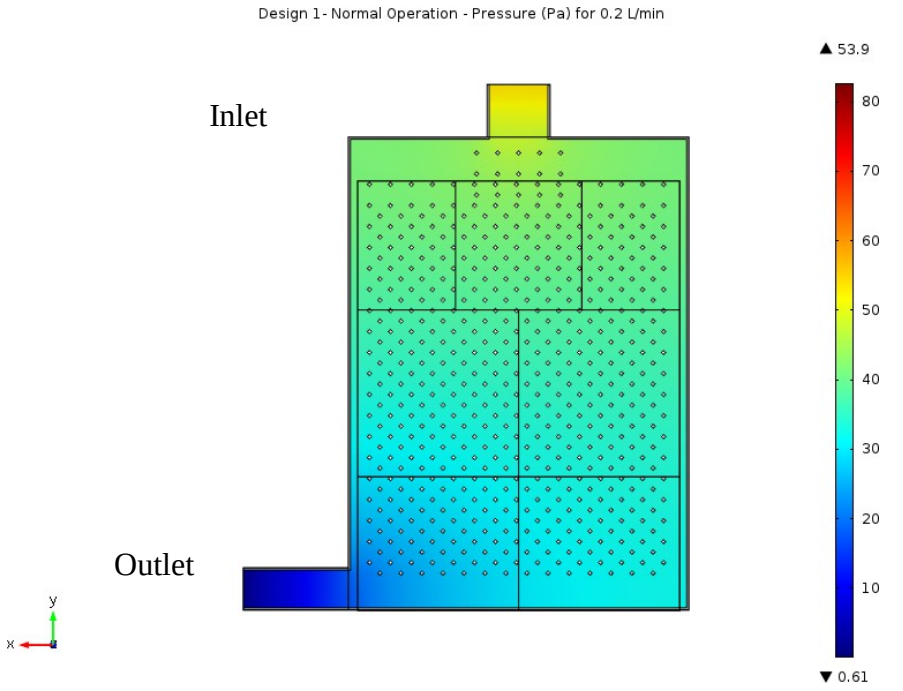

Fig. 9 (a). Design 1- Normal Operation – Pressure Distribution (Pa) for 0.2 L/min.

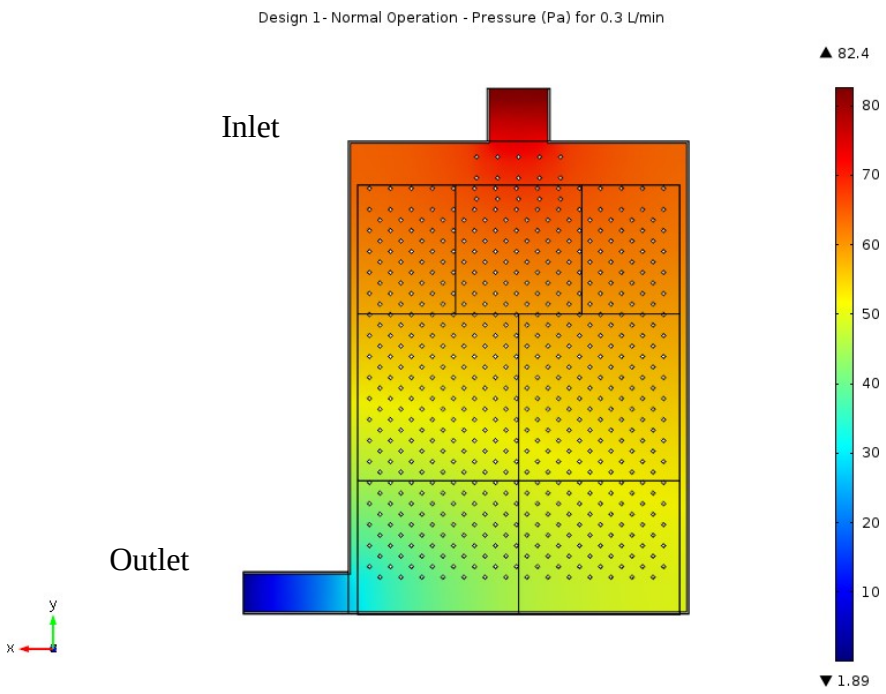

Fig. 9 (b). Design 1- Normal Operation – Pressure Distribution (Pa) for 0.3 L/min.

3.1.2 Normal Operation in Design 2

The second design was modelled based on mitigating the incompetency of the Design 1. The major concern of the Design 1 was the high pressure drop at the inlet.

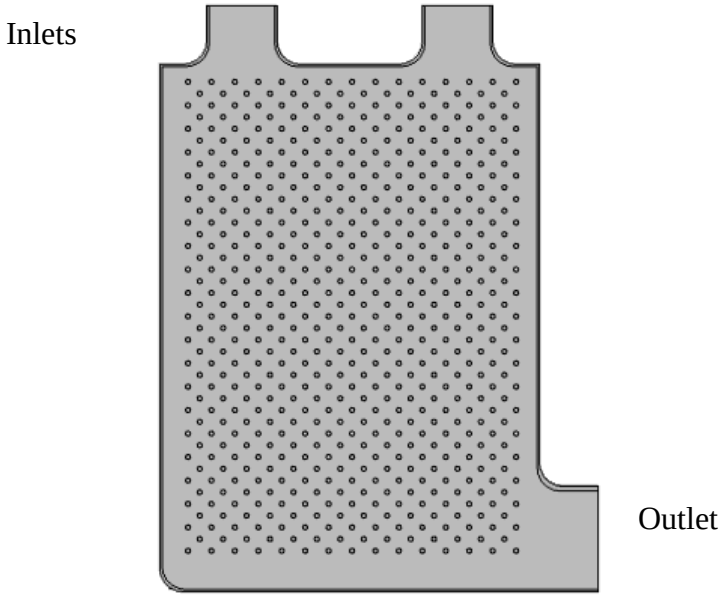

Fig. 10. Design 2 – sectioned front view.

To avoid high pressure drop values, a two inlet method was proposed with the same flow rate, thus dividing flow rate among two inlets can reduce the pressure drop as the pressure drop is directly proportional flow rate. The inlets were of same dimensions as Design 1 (i.e.) 30 mm x 25 mm and the outlet was 25 mm x 45 mm. The overall plate dimensions were kept constant (i.e.) 162 mm x 225 mm. The flow rate applied at the inlets was divided by 2, to keep the uniformity in all the simulations. In the Normal Operation, the plate is simulated for two flow rate (i.e.) 0.2 L/min and 0.3 L/min.

The surface temperature for Design 2 with flow rate 0.2 L/min and 0.3 L/min can be seen below. The maximum surface temperature for 0.2 L/min was 24.8°C at the bottom and for 0.3 L/min, the temperature was 23.3°C

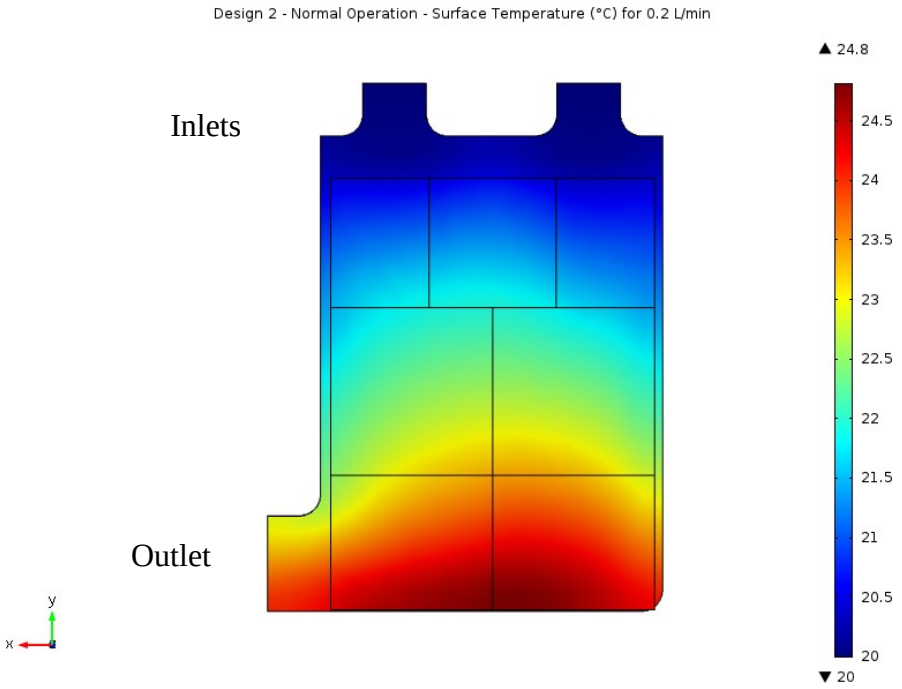

Fig. 11 (a). Design 2 - Normal Operation - Surface Temperature (°C) for 0.2 L/min.

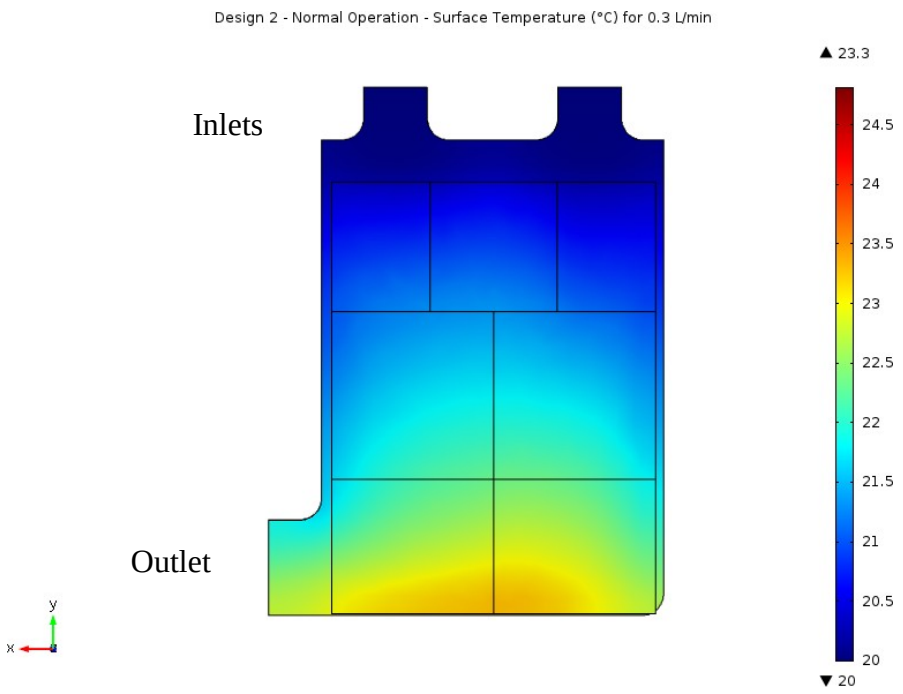

Fig. 11 (b). Design 2 - Normal Operation - Surface Temperature (°C) for 0.3 L/min.

The pressure distribution for Design 2 with flow rate 0.2 L/min and 0.3 L/min can be seen below.

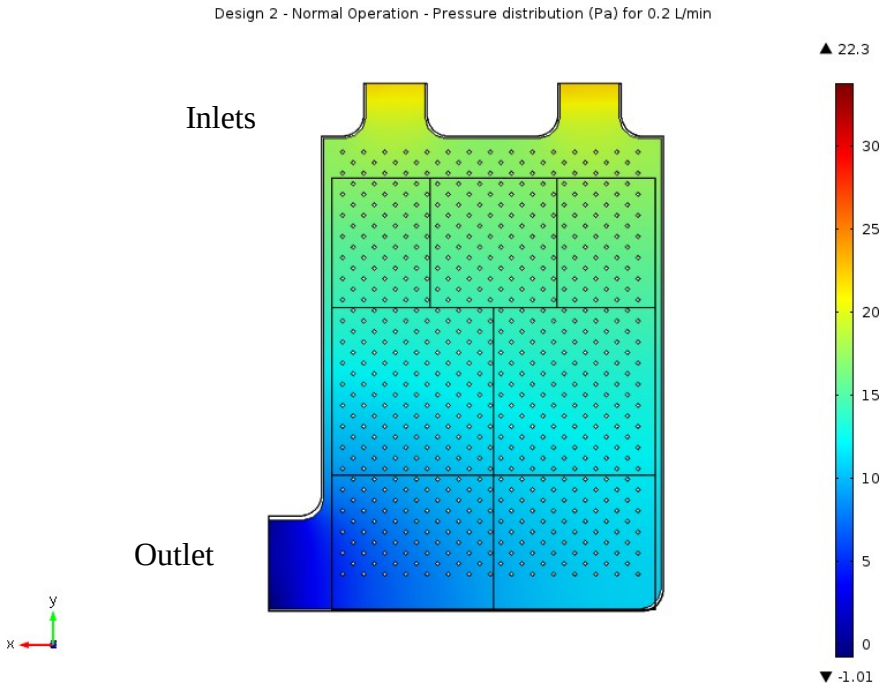

Fig. 12 (a). Design 2 - Normal Operation – Pressure distribution (Pa) for 0.2 L/min.

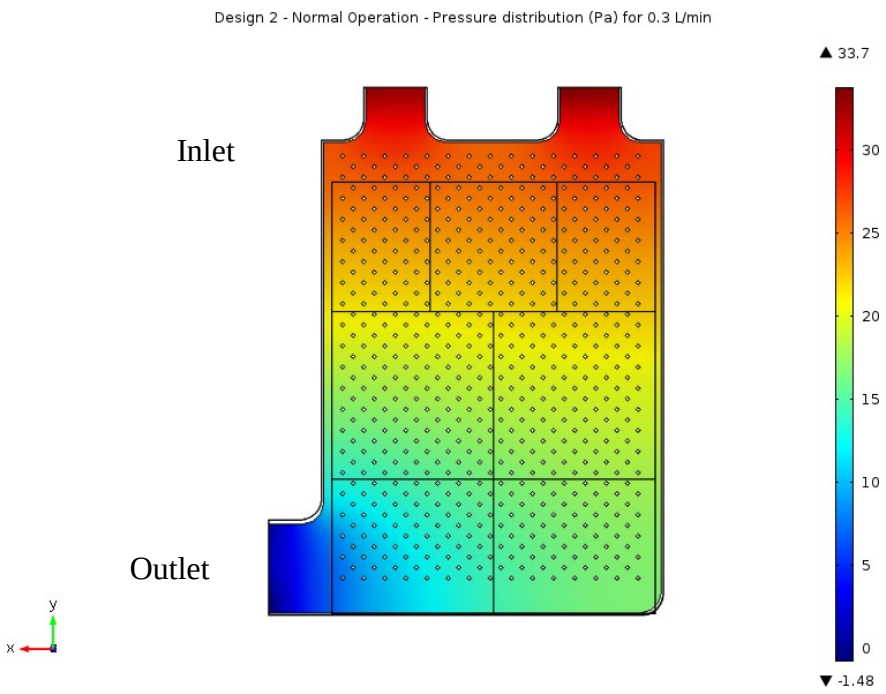

Fig. 12 (b). Design 2 - Normal Operation – Pressure distribution (Pa) for 0.3 L/min.

For 0.2 L/min, the pressure drop was 22.3 Pa and for 0.3 L/min, the pressure drop was 33.7 Pa.

3.1.3 Normal Operation in Design 3

After evaluating the results of Design 2, even though the two inlet method reduced the pressure drop during Normal Operation, it did not reduce the pressure drop as desired in the thermal runaway operation (can be seen in next section). Another concern with the two inlet method was running of two pipes and connectors from the pump to the plate. This would increase the cost as well as the weight of the battery pack. To reduce the pressure drop and the keep the number of pipes to one (1), a large inlet and outlet was proposed. The larger inlet provided for extra area for the fluid to enter the plate causing a reduction in the pressure drop. The size of inlet was increased to 80 mm x 25 mm and the outlet was increased to 30 mm x 60 mm.

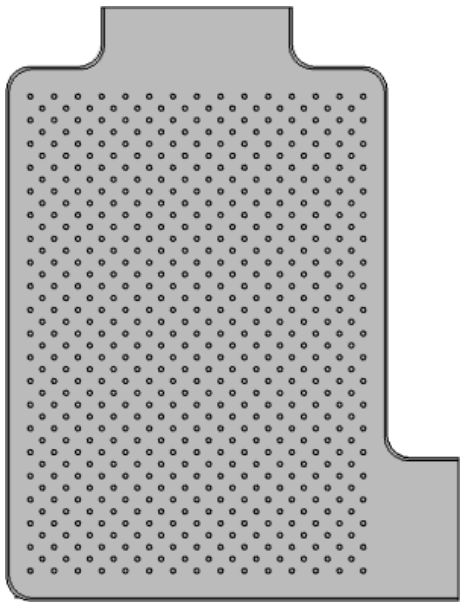

Fig. 13. Design 3 – sectioned front view.

The surface temperature for Design 3 with 0.2 L/min and 0.3 L/min can be seen below.

The maximum temperature for 0.2 L/min was 22.8°C and for 0.3 L/min was 21.9°C

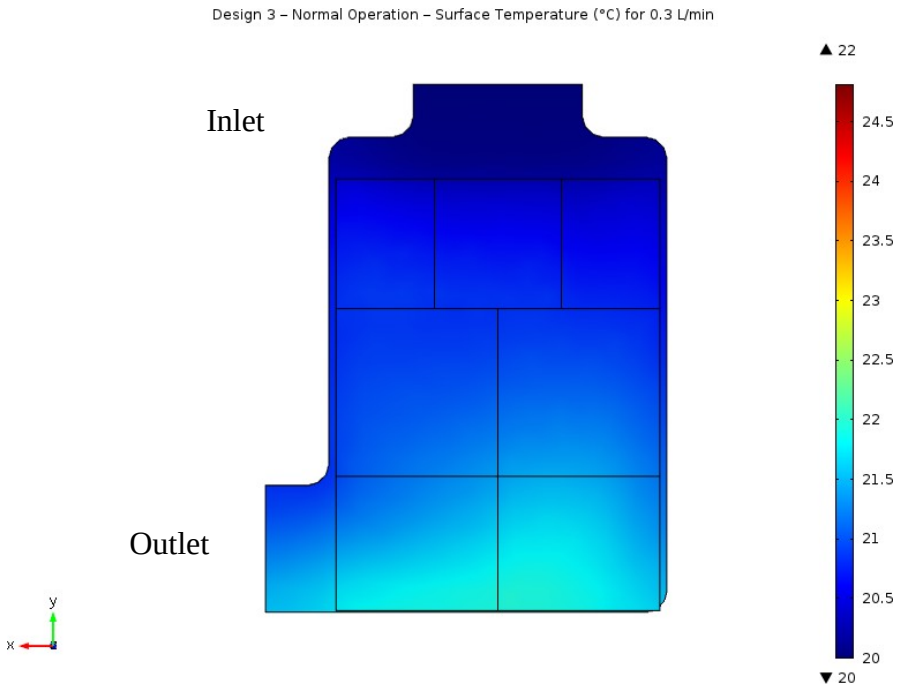

Fig. 14 (a). Design 3 – Normal Operation – Surface Temperature (°C) for 0.2 L/min.

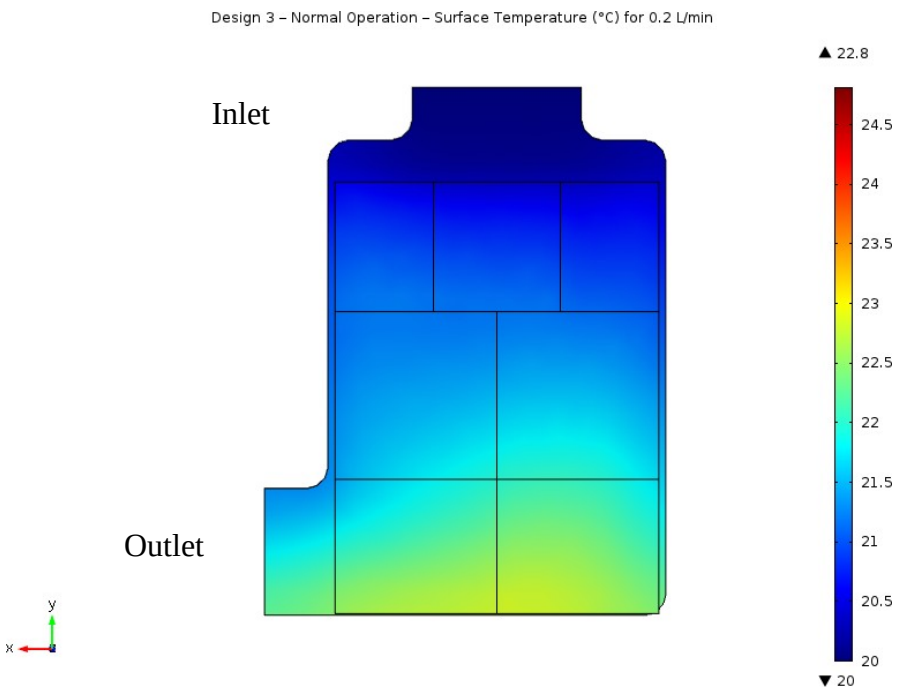

Fig. 14 (b). Design 3 – Normal Operation – Surface Temperature (°C) for 0.3 L/min.

The pressure distribution for Design 3 with 0.2 L/min and 0.3 L/min can be seen below. The pressure drop for 0.2 L/min was 21.4 Pa and for 0.3 L/min was 32.3 Pa.

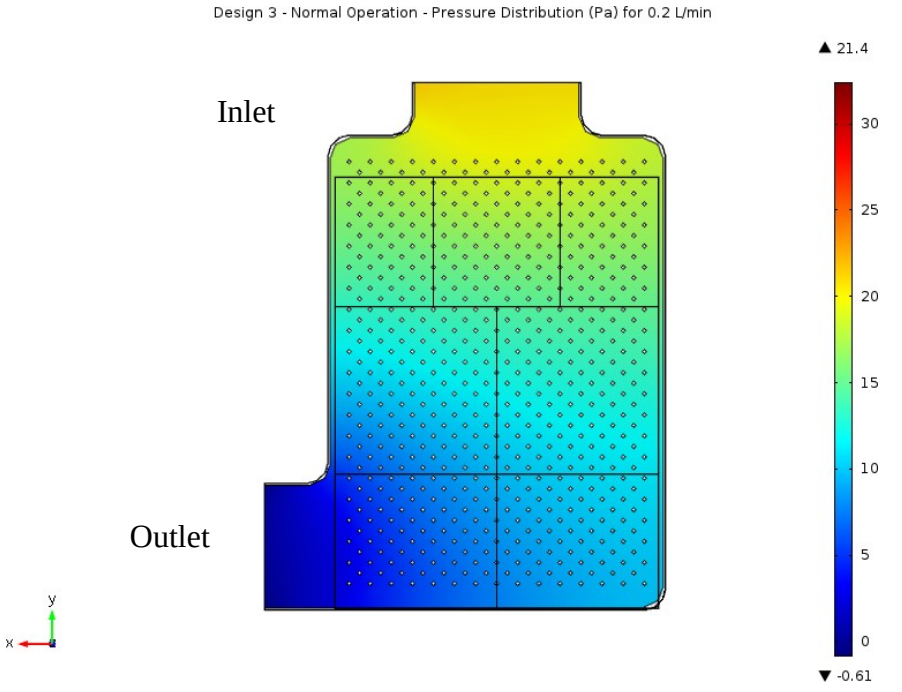

Fig. 15 (a). Design 3 - Normal Operation - Pressure Distribution (Pa) for 0.2 L/min.

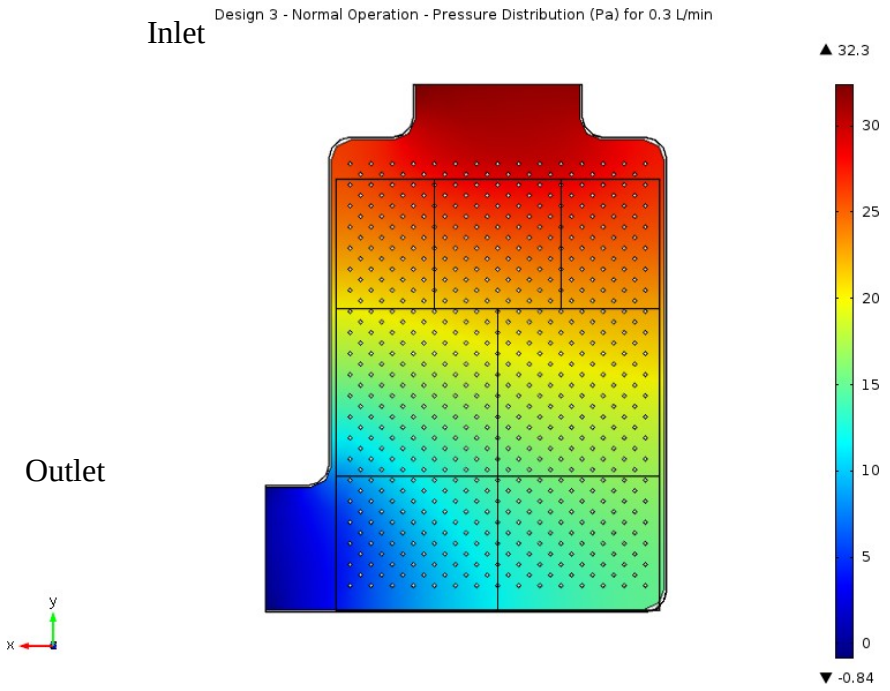

Fig. 15 (b). Design 3 - Normal Operation - Pressure Distribution (Pa) for 0.3 L/min.

3.2 Thermal Runaway

The thermal runaway was simulated as mentioned in the previous chapter with 100 MW/m^3 as heat and with flow rates of 20, 30, and 40 L/min. During thermal runaway, the temperature of the battery reaches to 1000°C within 10 seconds. From 0 to 200 seconds the battery was simulated normal operation. The thermal runaway starts at 200 seconds for 10 seconds and ends. The increased flow rate of 20, 30, and 40 L/min starts at 200 seconds and continues till the end of simulation at 230 seconds. The sudden rise in temperature can be seen in the surface temperature graphs at 200 seconds due to initialization of thermal runaway.

3.2.1 Thermal Runaway in Design 1

With the Design 1 and flow rate of 20 L/min, the surface temperature of the battery was maintained at 77°C. With 30 L/min, the battery temperature was maintained around

66.4°C and with 40 L/min, the battery temperature was kept at 63.1°C. The surface temperature variation can be seen in the figure below.

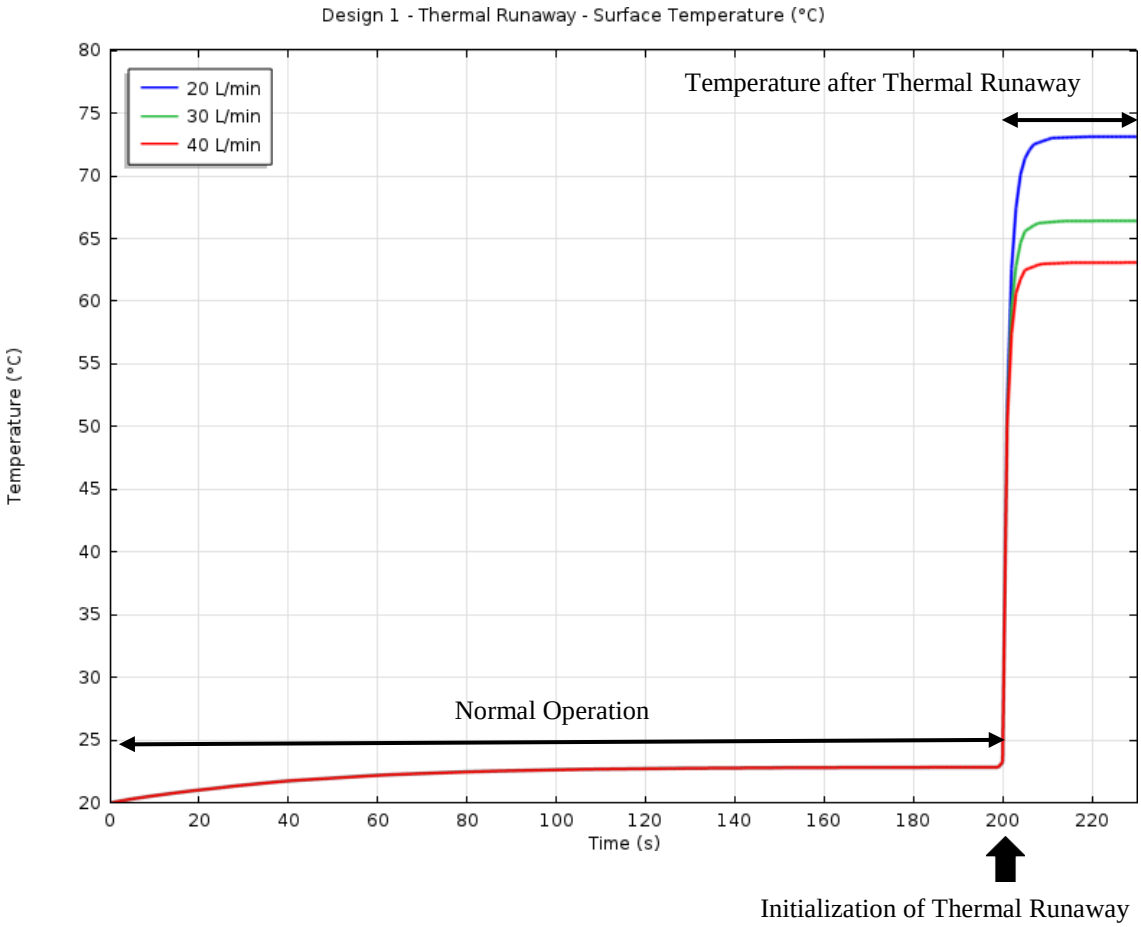

Fig. 16. Design 1 - Thermal Runaway - Surface Temperature (°C).

The pressure drop at the inlet for 20 L/min was 76.35 kPa (fig. 17 (a)) and for 30 L/min the pressure drop was 169.7 kPa (fig. 17 (b)). For 40 L/min, the pressure drop was 299.6 kPa (fig. 17 (c)). The maximum pressure values were visible at the start of the pins. With 20 L/min, the maximum pressure was 91.4 kPa. With 30 L/min, the maximum pressure was 204 kPa and with 40 L/min, the maximum pressure was 360 kPa. As the flow rate was increased, the maximum surface temperature on the battery decreased and the

pressure increased. The Design 1 was able to dissipate the heat generated in the thermal runaway but due to such high flow rates, the pressure drop at the inlet was extremely high.

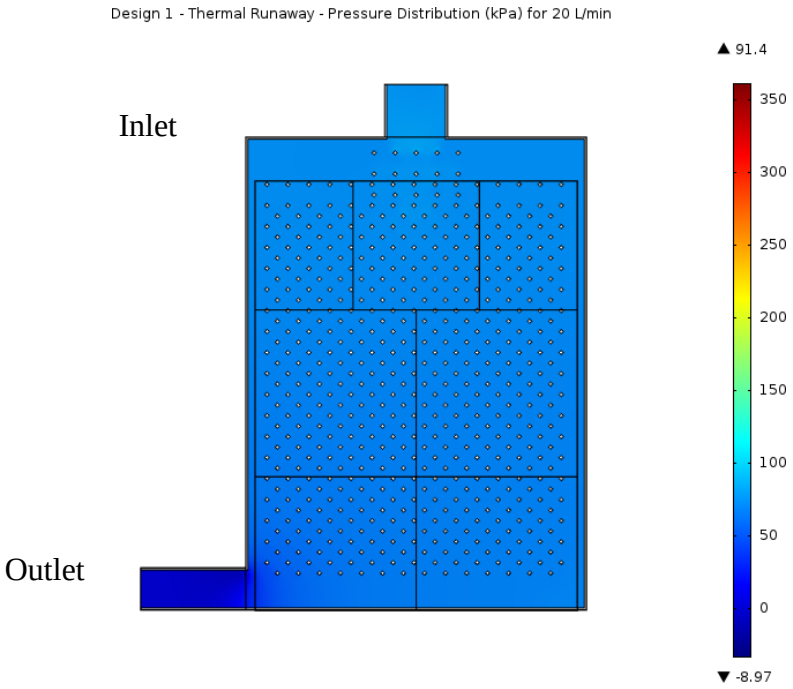

Fig. 17 (a). Design 1 - Thermal Runaway - Pressure Distribution (kPa) for 20 L/min.

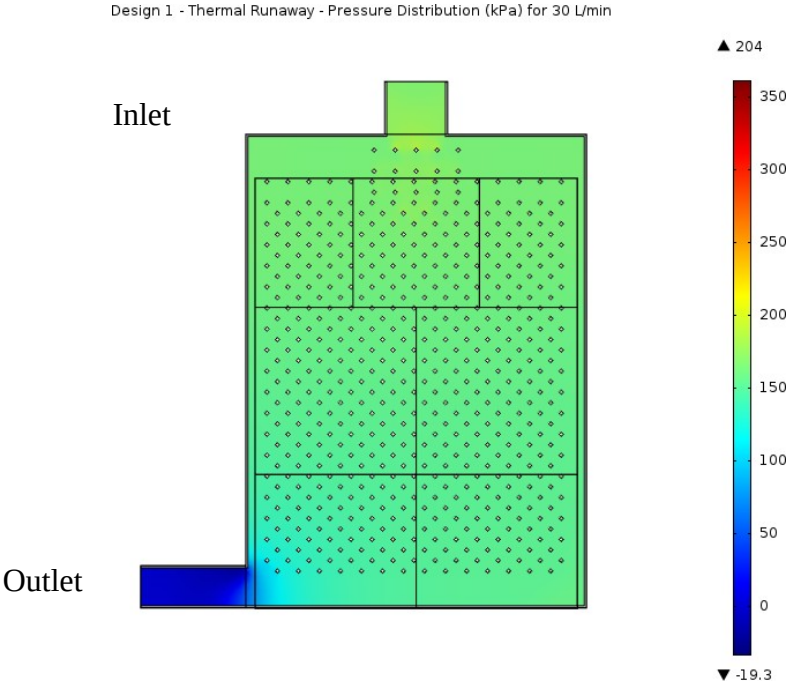

Fig. 17 (b). Design 1 - Thermal Runaway - Pressure Distribution (kPa) for 30 L/min.

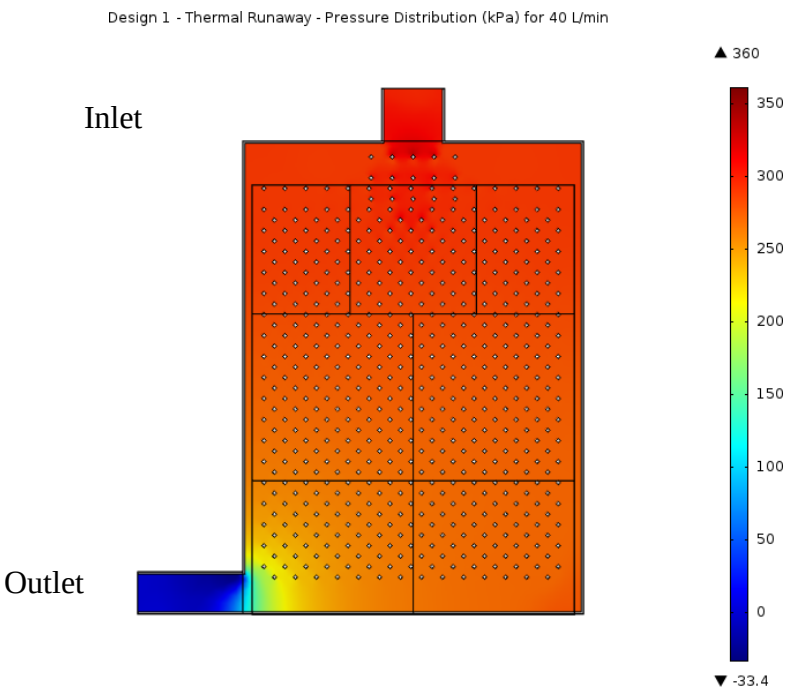

Fig. 17 (c). Design 1 - Thermal Runaway - Pressure Distribution (kPa) for 40 L/min.

3.2.2 Thermal Runaway in Design 2

The Design 2 was simulated as discussed in the previous chapter with flow rates of 20, 30 and 40 L/min. The maximum surface temperature was 93.2°C and the maximum pressure 30.5 kPa (fig. 19 (a)) can be seen when the fluid gets in contact with pins. The pressure drop at the inlets was 26.9 kPa. For 30 L/min, the maximum surface temperature was 60.5°C and the maximum pressure 66.9 kPa (fig. 19 (b)) is at start of pins, when the fluid get in contact with pins. The pressure drop at the inlets was 59.1 kPa. For 40 L/min, the maximum surface temperature was 57.3°C and the maximum pressure 117 kPa (fig. 19 (c)) is at start of pins, when the fluid get in contact with pins. The pressure drop at the inlets was 103.6 kPa.

The surface temperature and pressure distribution of Design 2 for thermal runaway with flow rate of 20, 30 and 40 L/min can be seen below.

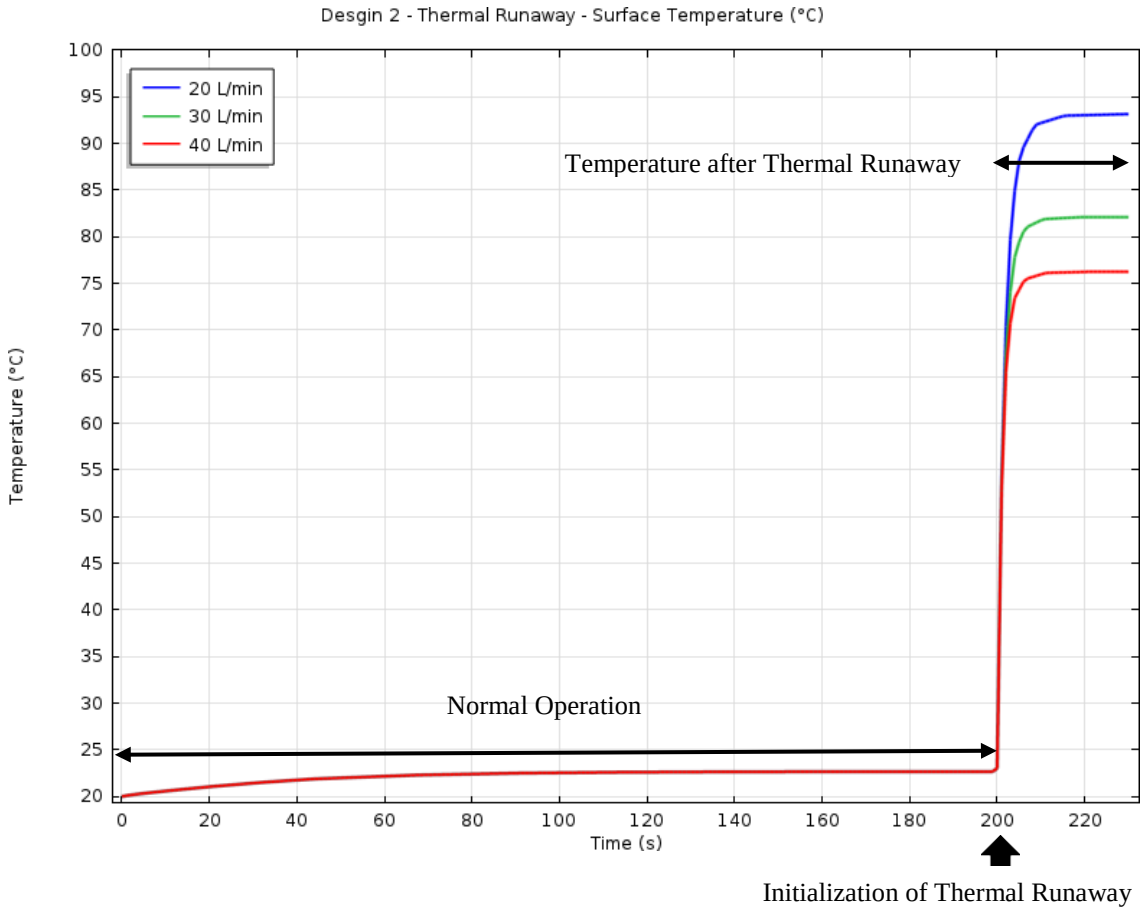

Fig. 18. Design 2 - Thermal Runaway - Surface Temperature (°C) for 20 L/min

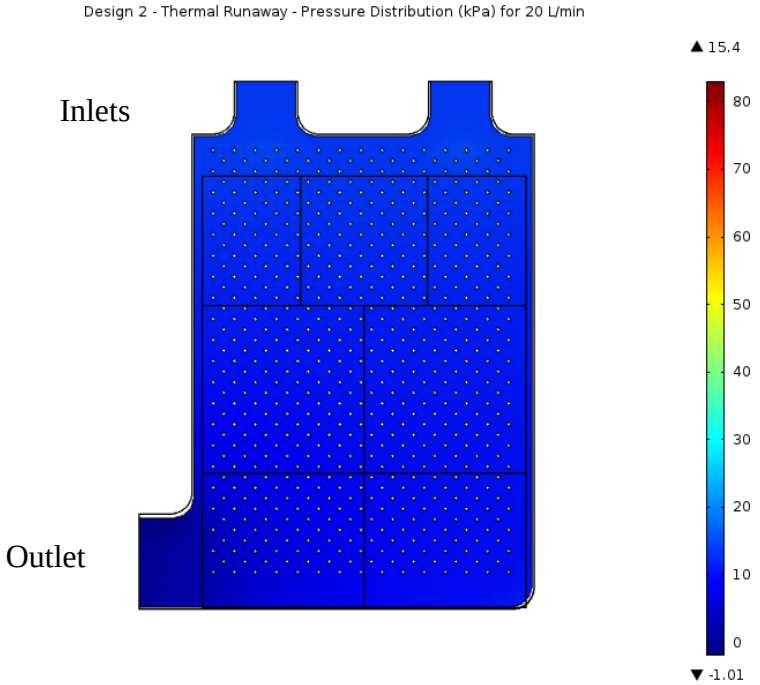

Fig. 19 (a). Design 2 - Thermal Runaway - Pressure Distribution (kPa) for 20 L/min

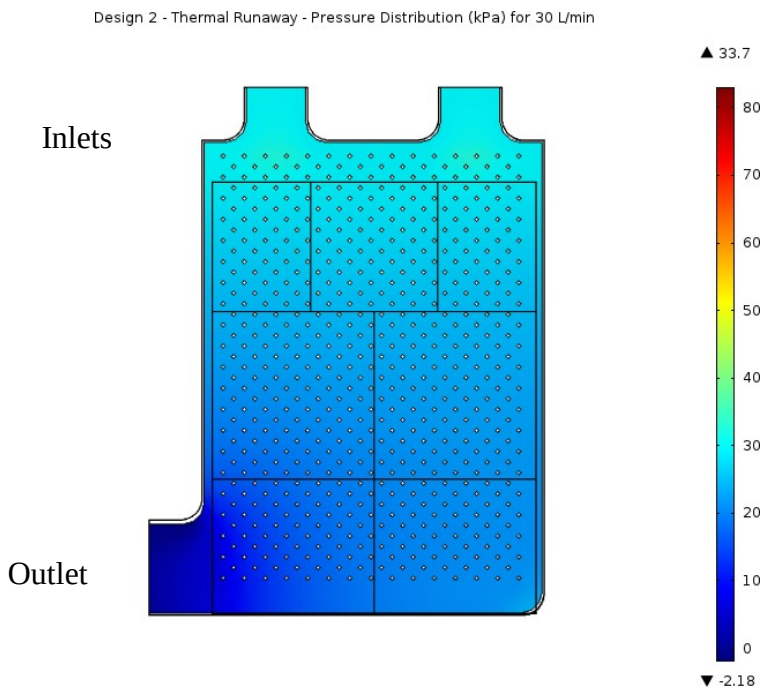

Fig. 19 (b). Design 2 - Thermal Runaway – Pressure Distribution (kPa) for 30 L/min

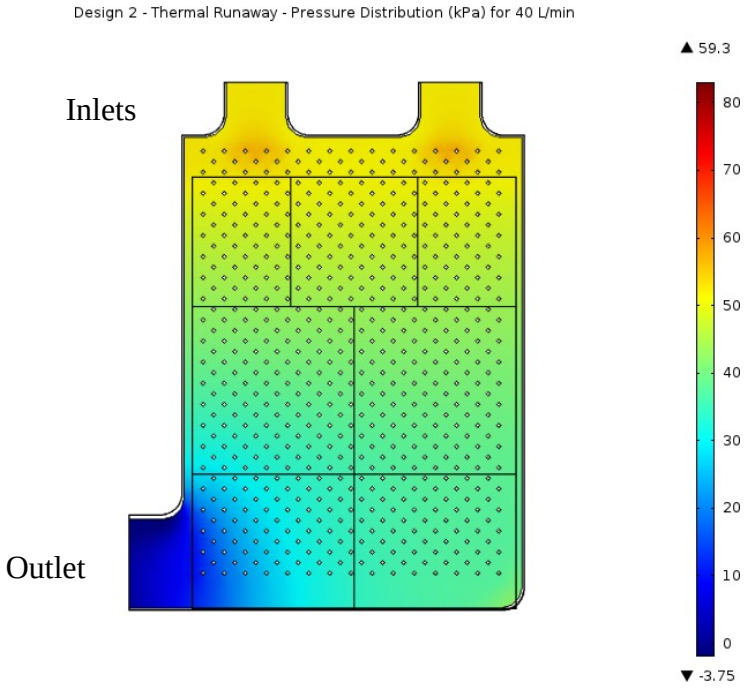

Fig. 19 (c). Design 2 - Thermal Runaway – Pressure Distribution (Pa) for 40 L/min

3.2.3 Thermal Runaway in Design 3

The thermal runaway in Design 3 was simulated as mentioned in the previous chapter with 100 MW/m^3 heat and with flow rates of 20, 30, and 40 L/min for 30 seconds. With the Design 3 and flow rate of 20 L/min, the surface temperature of the battery was maintained at 76.7°C. With 30 L/min, the battery temperature was maintained around 70.8°C and with 40 L/min, the battery temperature was kept at 67.8°C. The surface temperature variation can be seen in the figure below.

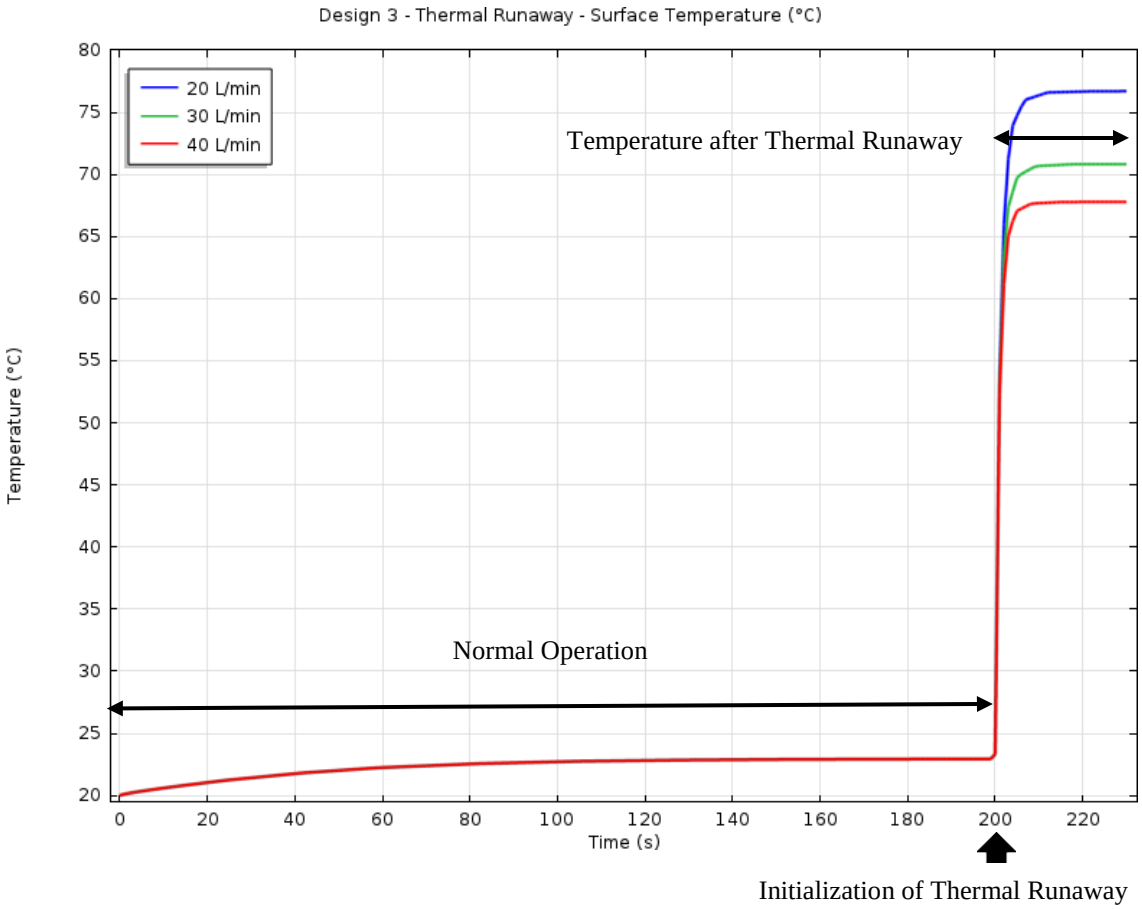

Fig. 20. Design 3 - Thermal Runaway - Surface Temperature (°C) for 20 L/min.

For 20 L/min, the maximum pressure 21.2 kPa (fig. 21 (a)) can be seen when the fluid get in contact with pins while the pressure drop at the inlet was 18.8 kPa.

For 30 L/min, the maximum pressure 46.9 kPa (fig. 21 (b)) is at start of pins, when the fluid get in contact with pins while the pressure drop at the inlet was 41.7 kPa. For 40 L/min, the maximum pressure 82.8 kPa (fig. 21 (c)) and the pressure drop at the inlet was 73.5 kPa. The pressure distribution for Design 3 can be seen below.

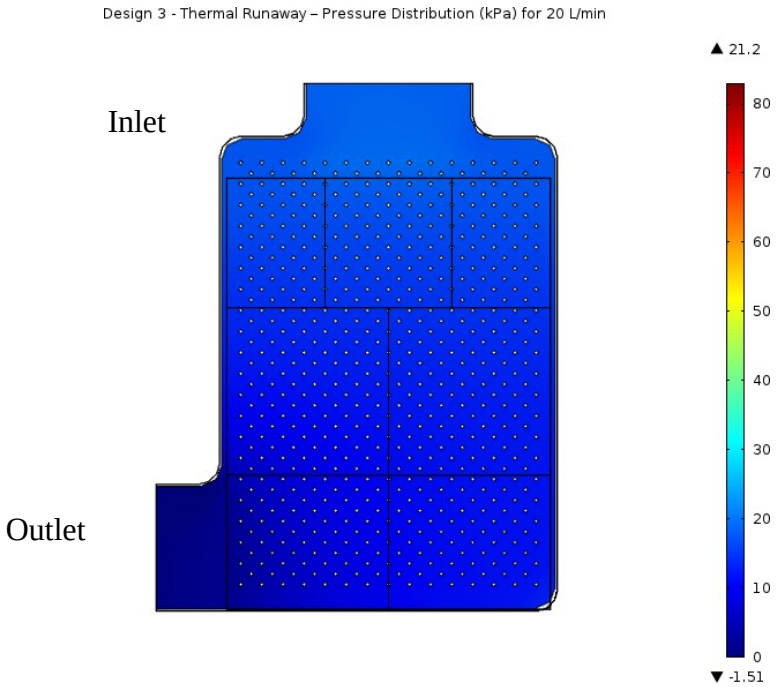

Fig. 21 (a). Design 3 - Thermal Runaway - Pressure Distribution (kPa) for 20 L/min.

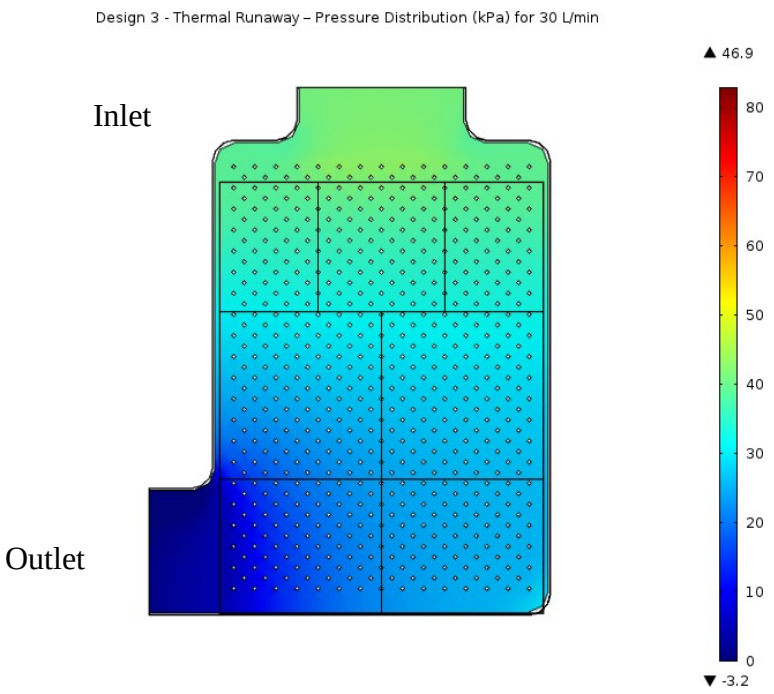

Fig. 21 (b). Design 3 - Thermal Runaway – Pressure Distribution (kPa) for 30 L/min

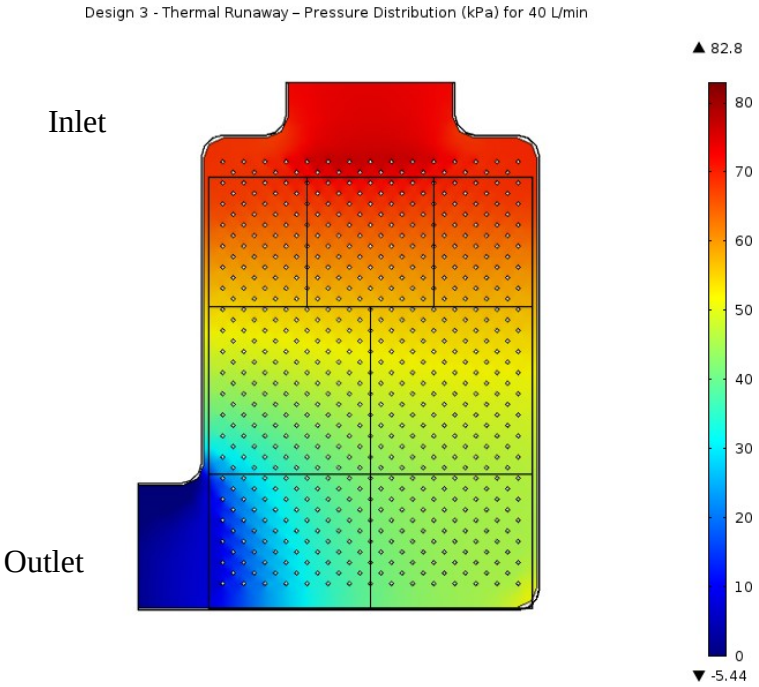

Fig. 21 (c). Design 3 - Thermal Runaway – Pressure Distribution (kPa) for 40 L/min.

3.3 Comparison of Cooling Plates

Although the designs were improvements of the previous designs, but the comparison was essential for selection of the best design. The three cooling plates namely Design 1, Design 2 and Design 3 were simulated with the same initial conditions and flow rates during both the operations. The selection of the best design was based on the following points.

- Ability to maintain the battery surface temperature below 25°C during normal operation.
- Ability to dissipate maximum heat and keep the temperature as low as possible during thermal runaway.
- Ability to have least pressure drop at the inlet during both the Normal Operation and thermal runaway operations.

A comparative study was done on the three cooling plates on the basis of above mentioned criteria. The data was collected from the simulation results and analyzed separately. The below table show the comparison of the three cooling plates for maximum battery surface temperature and pressure drop during normal operation.

Table 6. Comparison of cooling plates for Normal Operation.

	Maximum Surface Temperature (°C)		Pressure drop (Pa)	
Flow Rate (L/min)	0.2	0.3	0.2	0.3
Design 1	22.7	21.9	53.9	82.4
Design 2	24.9	23.3	22.3	33.7
Design 3	22.8	21.9	21.4	32.3

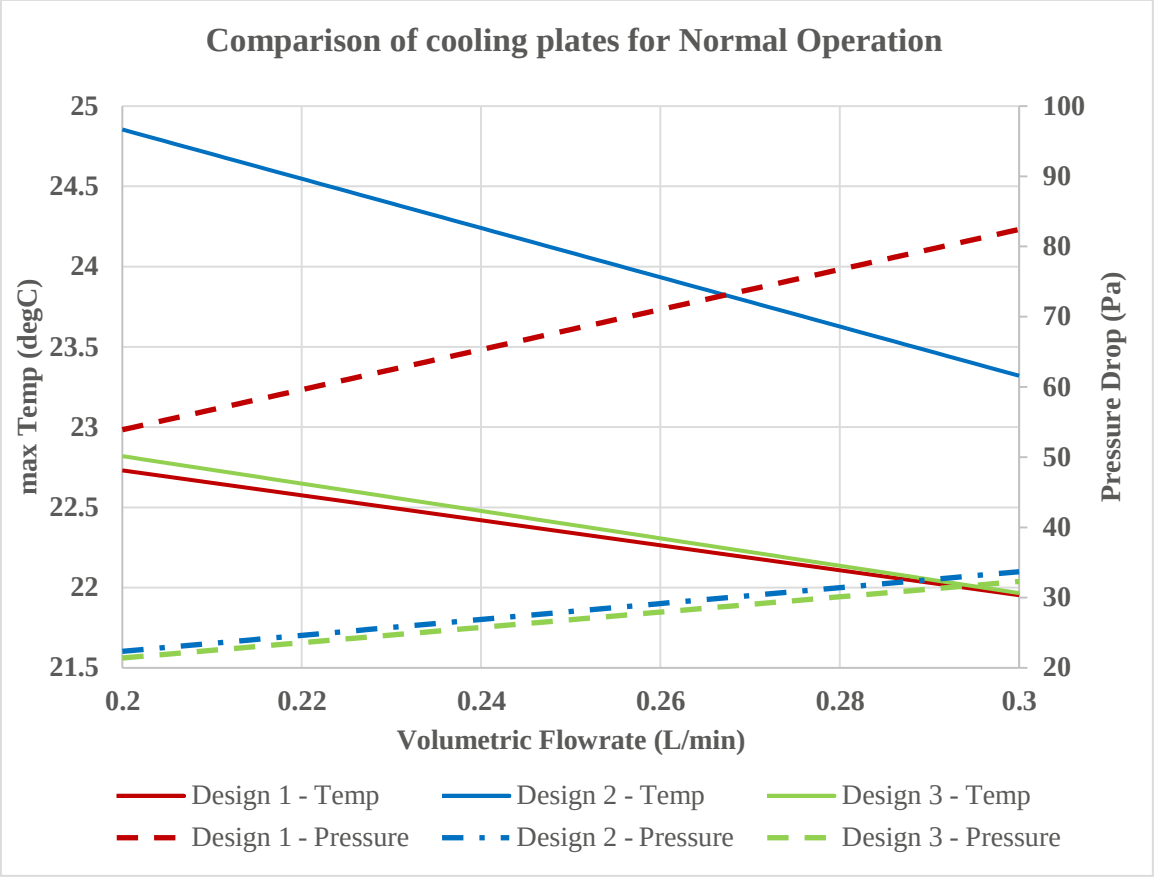

Fig. 22. Comparison of cooling plates for Normal Operation.

The surface temperature for the three designs for different flow rate is below 25°C with not much difference among the three designs. The pressure drop for Design 2 is very less compared to the Design 1, showing a clear improvement in the design. The pressure drop values for Design 2 and Design 3 are in very close proximity to each other and the pressure drop Design 3 is comparatively less than Design 2.

From the above analysis, few points can be concluded:

- Design 1 and Design 3 showed similar surface temperature curve and maintained a lower surface temperature in comparison with Design 2.
- The pressure drop is least in Design 3, due to increased surface area at the inlet.

- Among the three designs, Design 3 satisfies the design criteria more aptly with a balance between the surface temperature and pressure drop.

A similar study was done for the thermal runaway. The table below shows the comparative study of the three designs.

Table 7. Comparison of cooling plates for Thermal Runaway

	Maximum Surface Temperature (°C)			Pressure drop (kPa)		
Flow rate (L/min)	20	30	40	20	30	40
Design 1	73.1	66.4	63.0	76.3	169.7	299.6
Design 2	93.1	82.1	76.2	13.7	29.9	52.4
Design 3	76.7	70.8	67.8	18.8	41.7	73.5

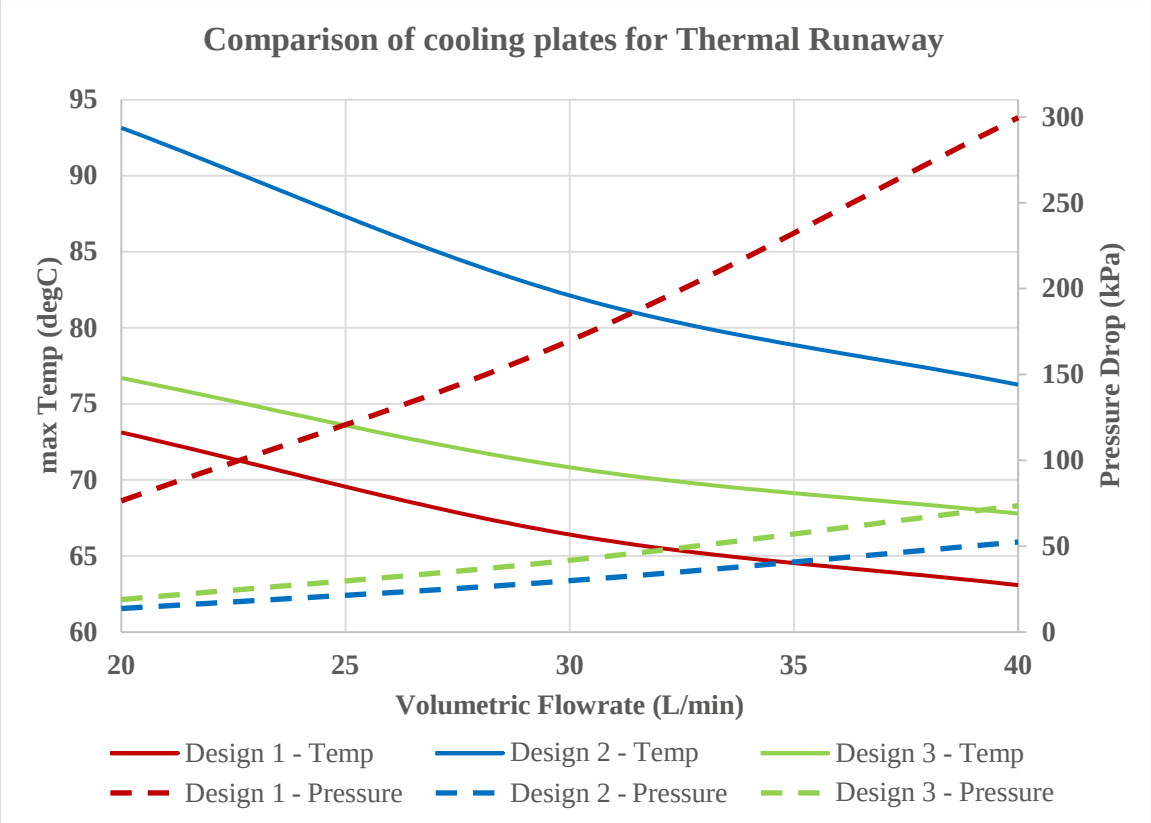

Fig. 23. Comparison of cooling plates for Thermal Runaway

From the above table and figure, the following points can be concluded:

- Temperature of the battery surface decreases with the increase in flow rate.
- Pressure drop increases with increase in flow rate.
- The pressure drop in Design 2 is least among all the designs.
- Design 3 maintains lower temperatures when compared to other designs.

From the above analysis, Design 3 was concluded to be the best design in terms of both surface temperature and pressure drop properties. Design 3 had the lesser pressure drop values at the inlet with least surface temperature when compared with the rest of the designs.

3.4 Validation of the model through Numerical Methods

To validate the simulation conducted, the well-known Darcy-Weisbach equation was utilized to calculate and verify the pressure drop in the cooling plates.

$$\Delta pp = ffDD \times \frac{\rho\rho}{2} \times \frac{vv^2}{DD_h} \times LL$$

(15)

The hydraulic diameter and velocity are calculated with the initial conditions. Length (l), width (w) are dimensions of the channel/inlet.

$$VVVVVVVVVVVttVV\,(vv) = \frac{MMMMssss\,FFVVVVFF\,rrMMttVV\left(\frac{kkkk}{ss}\right)}{(\rho\rho \times AArrVVMM\ VVff\ CC\boldsymbol{h}_{MMaaaalVVV})}$$

(16)

$$HHVVHHrrMMHHWWVV\ DDVVMMmmVVttVVrr\ (DD_h) = \frac{2 \times VV \times FF}{VV + FF}$$

(17)

The friction factor was calculated using the analogy for laminar flow:

$$ff_{DD}\ xx\ RRVV = 64$$

(18)

The verification for pressure drop for Design 3 during normal operation was calculated.

Table 8. Comparison of pressure drop from calculation and simulation for Design 3

Flow Rate (L/min)	Calculated Pressure Drop (Pa)	Pressure Drop from simulation (Pa)	Percentage Difference (%)
0.2	17.8	22.3	19.9
0.3	39.6	33.6	18.1

From the above table, the percentage difference in the values obtained from calculating pressure drop by Darcy-Weishbach equation and from the simulation performed is less than 20%. The values are acceptable as it is very difficult to calculate the exact pressure drop for such a complex problem.

CHAPTER 4

OPTIMIZATION OF FINAL DESIGN AND MANUFACTURING

After the selection of Design 3 as the final design, an optimization process was conducted to maximize the efficiency of the plate. This was done by changing the pin diameter and the thickness of the plate. The results of the studies are discussed below.

4.1 Effect of Pin diameter on cooling plates

The pin diameter for all the analysis done in the previous chapter was kept constant at 1 mm. Three different pin diameter were chosen namely 1 mm, 1.5 mm and 2 mm. The overall dimension of the cooling plate was kept same to maintain the design uniformity. The plates were simulated for the flow rates of 0.2 L/min and 0.3 L/min for Normal Operation.

Table 9. Comparison of pin diameter for Normal Operation

	Maximum Surface Temperature (°C)		Pressure Drop (Pa)	
Flow Rate	0.2 L/min	0.3 L/min	0.2 L/min	0.3 L/min
1mm	22.8	21.9	21.4	32.3
1.5mm	22.6	21.7	10.5	19.4
2mm	22.5	21.7	22.8	34.3

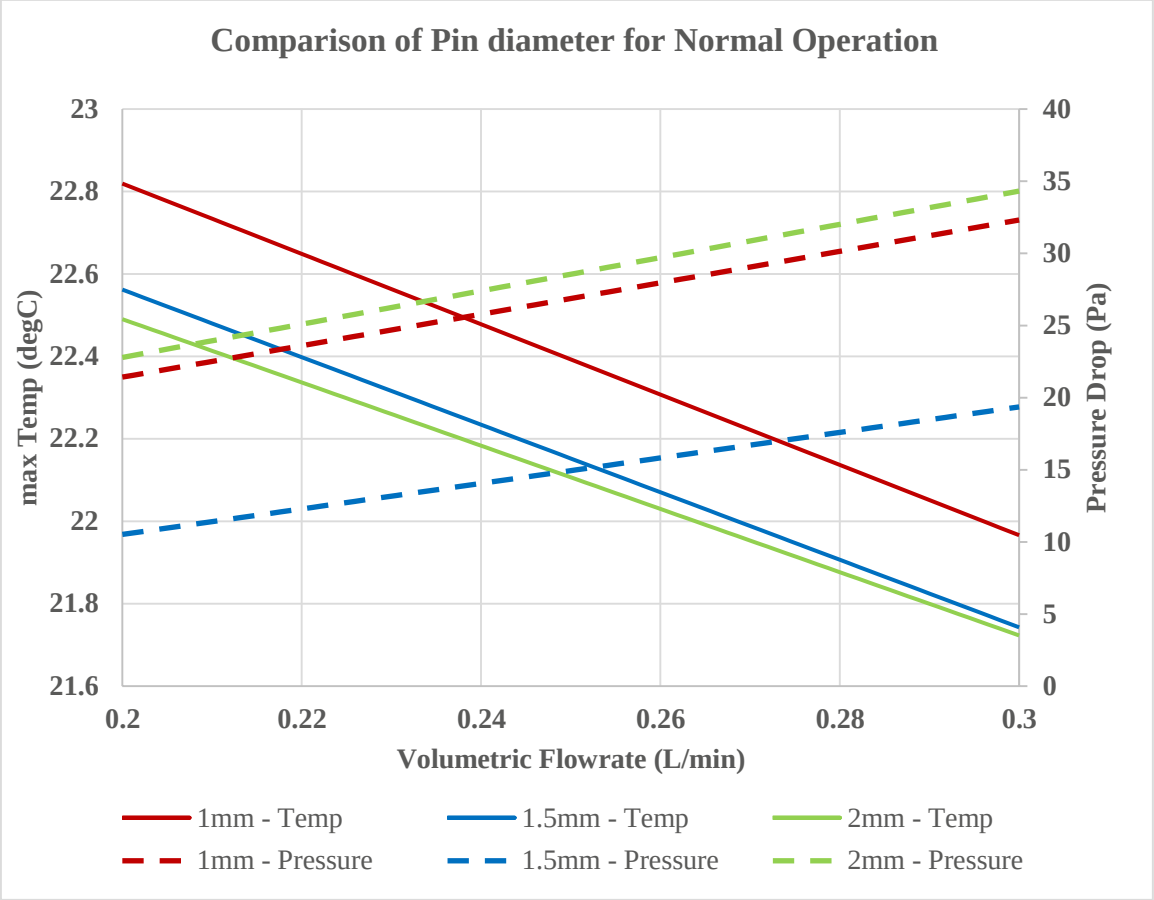

Fig. 24. Comparison of Pin diameter for Normal Operation.

From the above table and figure, it can be concluded that the change in pin diameter did not affect the surface temperature significantly. However, the pressure drop for 1.5 mm was visibly less compared to 1mm and 2mm pin diameter.

For the consensus, the thermal runaway simulation was also performed on the three pin diameters with 20, 30 and 40 L/min flow rates. In the below table and figure, the change in pin diameter did not have a significant impact on the surface temperature of battery but the pressure drop varied drastically. The pressure drop increased with increasing diameter and flow rate. The pin diameter of 1mm had the least pressure drop among all the other

diameters. It can be concluded that the 1mm diameter is best option for both normal operation and thermal runaway operations.

Table 10. Comparison of pin diameter for Thermal Runaway

	Maximum Surface Temperature (°C)			Pressure drop (kPa)		
Flow rate	20 L/min	30 L/min	40 L/min	20 L/min	30 L/min	40 L/min
1mm	76.7	70.8	67.8	18.8	41.7	73.5
1.5mm	72.3	67.2	64.0	28.9	61.4	105.8
2mm	73.5	67.8	64.9	42.2	93.2	163.9

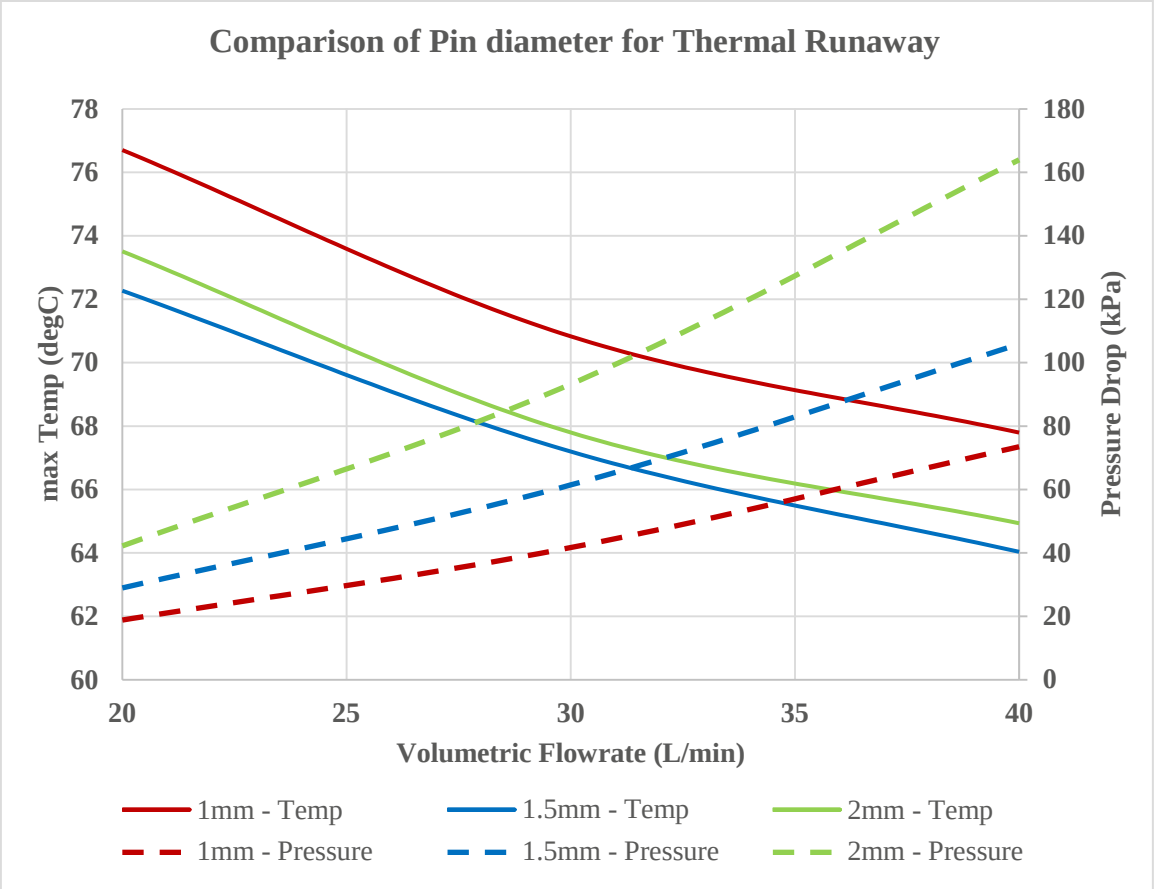

Fig. 25. Comparison of Pin diameter for Thermal Runaway.

4.2 Effect of thickness of plate on cooling plates

In the previous chapter, all the simulation were performed with 1mm thickness. The thickness of the cooling plates was changed from 1mm to 2mm to verify the impact of thickness on the cooling abilities of the plates. The plate was simulated with two thickness accordingly as discussed in the previous chapters for normal operation and thermal runaway.

Table 11. Comparison of thickness of plate for Normal Operation

	Maximum Surface Temperature (°C)		Pressure Drop (Pa)	
Flow rate	0.2 L/min	0.3 L/min	0.2 L/min	0.3 L/min
1mm	22.8	21.9	21.4	32.3
2mm	22.8	21.9	17.7	26.7

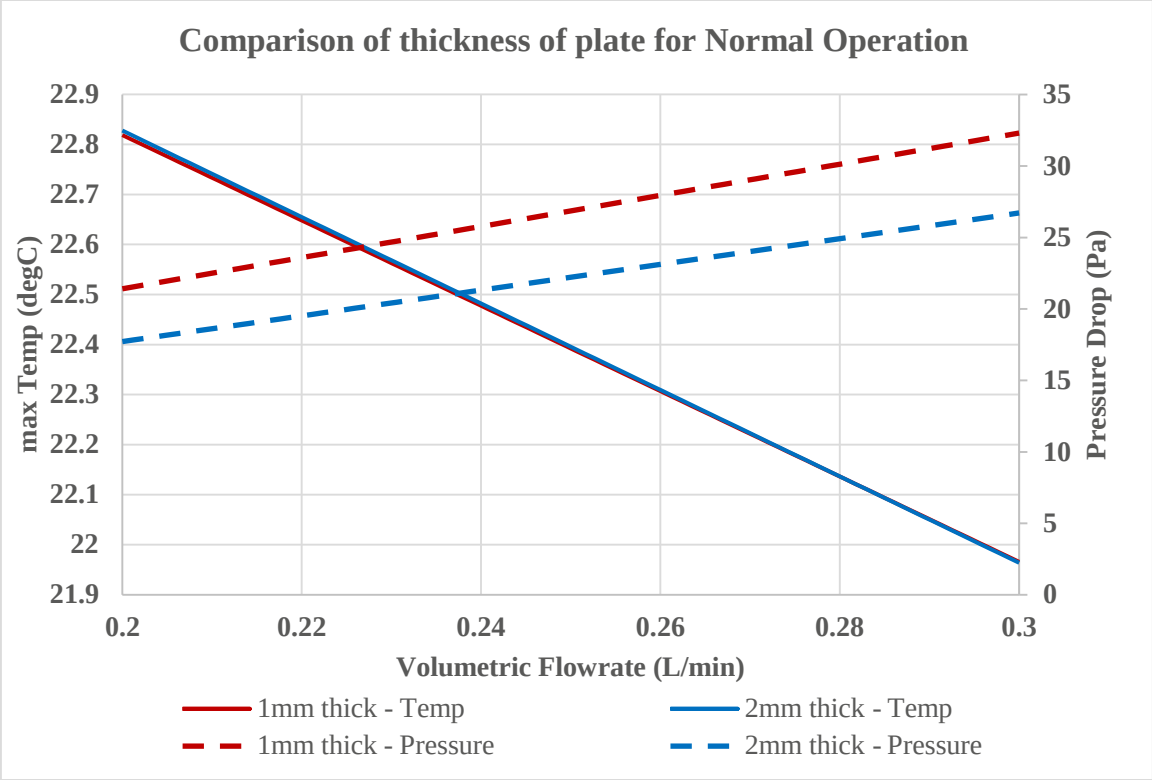

Fig. 26. Comparison of thickness of plate for Normal Operation.

From the above table and figure, the thickness of the plate did not affect the surface temperature. However, the pressure drop was decreased by a small margin. The thermal runaway results for different thickness are listed below.

Table 12. Comparison of thickness of plate for Thermal Runaway

	Maximum Surface Temperature (°C)			Pressure drop (kPa)		
Flow rate	20 L/min	30 L/min	40 L/min	20 L/min	30 L/min	40 L/min
1mm	76.7	70.8	67.8	18.8	41.7	73.5
2mm	76.4	70.2	66.8	26.9	59.1	103.34

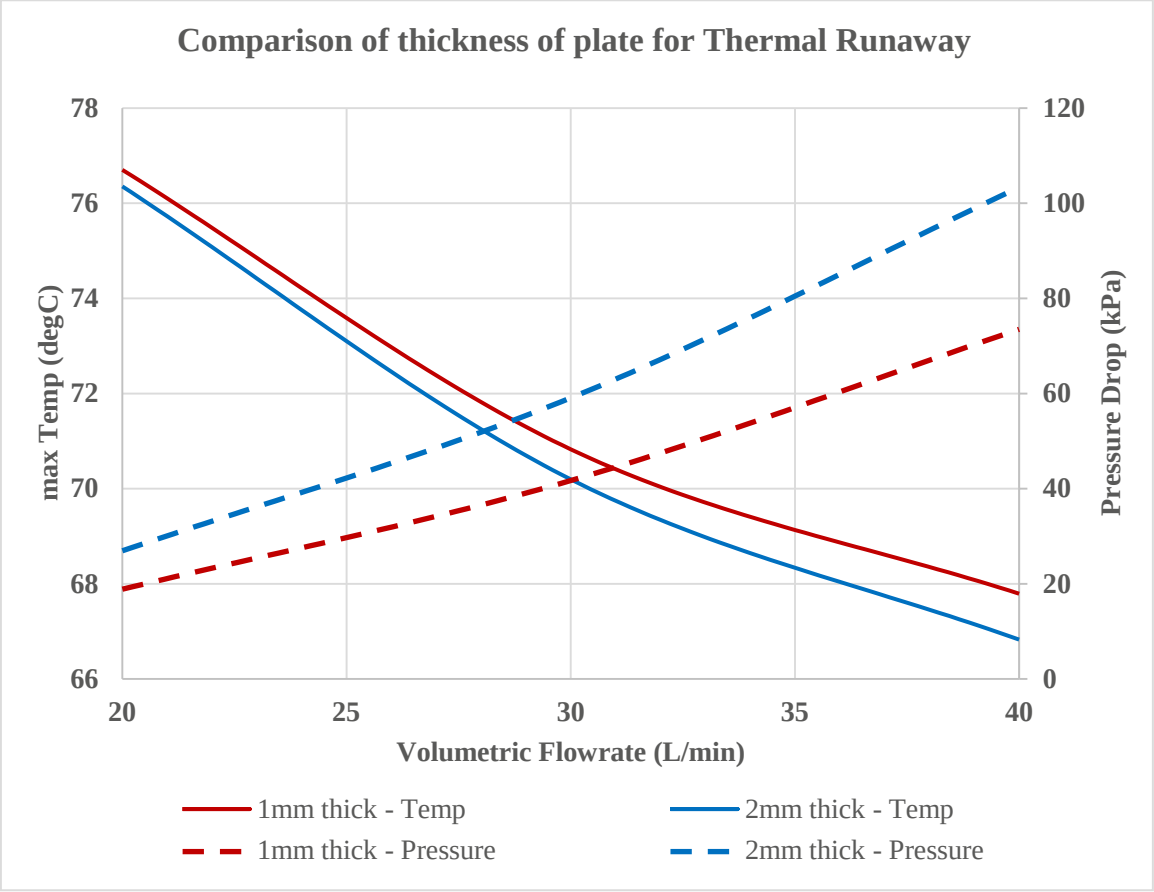

Fig. 27. Comparison of thickness of plate for Thermal Runaway.

From the above table and figure, the increase in thickness of the plate did not affect the surface temperature after thermal runaway. The pressure drop increased with the increase in flow rate and thickness. From the above two results, the thickness of 1mm is better than 2mm. The thickness was also not changed considering the overall dimensions of the battery pack. The increase in the thickness of the plate will increase the overall dimensions and weight of the battery pack and to avoid this, the thickness of the plate was restricted to 1mm.

4.3 Structural Analysis of the Plate

After the finalization of thickness and pin diameter, a study was performed to determine the structural integrity of the design. A fluid solid interaction (FSI) method was used on the cooling plate to determine the stress induced caused by the flow of water inside the plate. The outer surface of the plate was constrained replicating the condition of plate in battery packs. The flow rate of 50 L/min was used for the flow, giving a factor of safety for the design, as the maximum flow rate used in the previous simulations was 40 L/min. The maximum stress was generated at the edges of the plate, were the plate was welded and bended.

Table 13. Boundary Condition for Stress analysis

Entity	Location
Fixed Constraint	Outer surface of plate
Pressure from fluid	Inner surface of plate
Flow rate	50 L/min

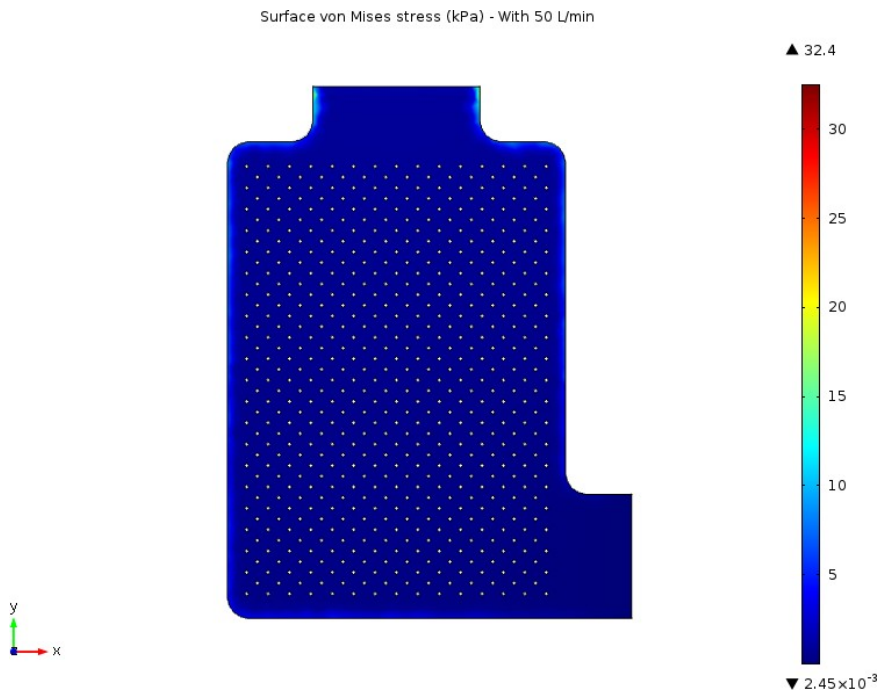

Fig. 28 (a). Stress Analysis of the cooling plate.

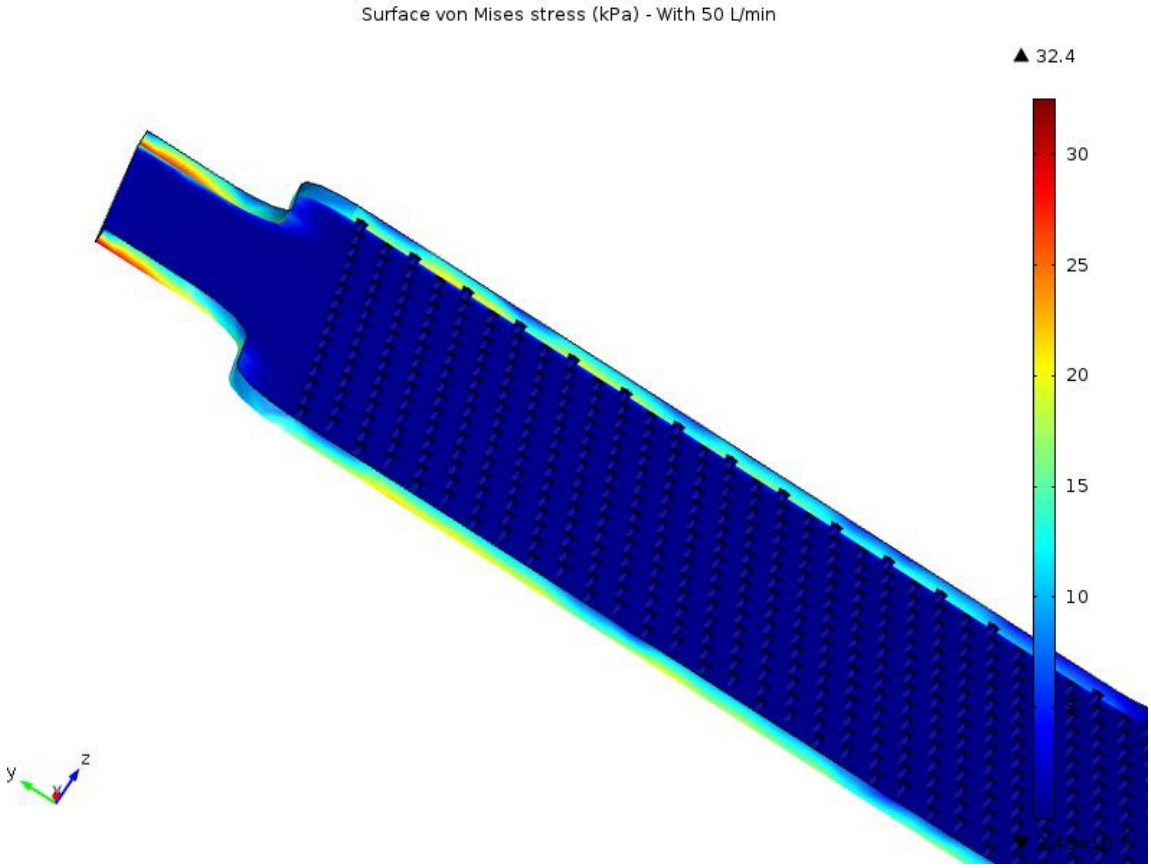

Fig. 28 (b). Maximum Stress areas of the cooling plate.

The maximum stress generated due to flow of fluid inside the plate with the flow rate of 50 L/min was 32.4 kPa. The ultimate tensile strength of aluminum 6063 is 241 MPa. The pressure developed by the flow of fluid in the cooling plate is very much less than the ultimate tensile strength, giving a very high factor of safety for the design.

4.4 Modal Analysis

A modal analysis was performed on the plate to determine the mode shapes of the cooling plate. Modal analysis is performed to test the structures under vibrational excitation. The dynamic response of the structure is studied during excitation. The plate was constrained as shown in the figure 29 on both the sides and was allowed to vibrate at its own natural frequency. The deformed mode shapes of the natural frequency of the plate are listed below. The sides of the plate were constrained as show in Fig. and was allowed to vibrate freely.

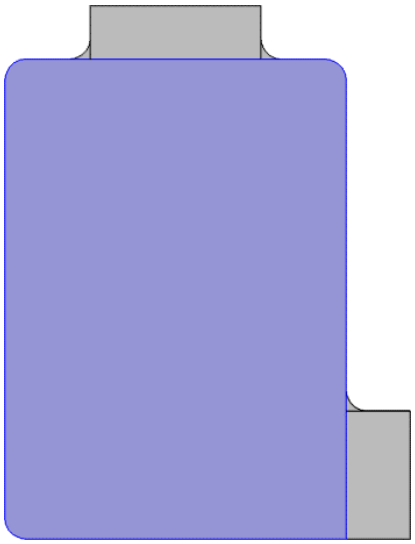

Fig. 29. Constraints for the modal analysis. Sides of the plate are fixed to replicate the actual battery pack.

The first natural frequency of Li-ion battery was observed to be 274 Hz by Choi et al [36]. The first Eigen frequency of Design 3 was 1873 Hz. The first six Eigen frequencies and deformed shapes of Design 3 are listed below.

Table 14. First six Eigen frequency of Design 3

Mode Shape	Eigen frequency (Hz)
1	1873
2	1885
3	2032
4	2038
5	3226
6	3255

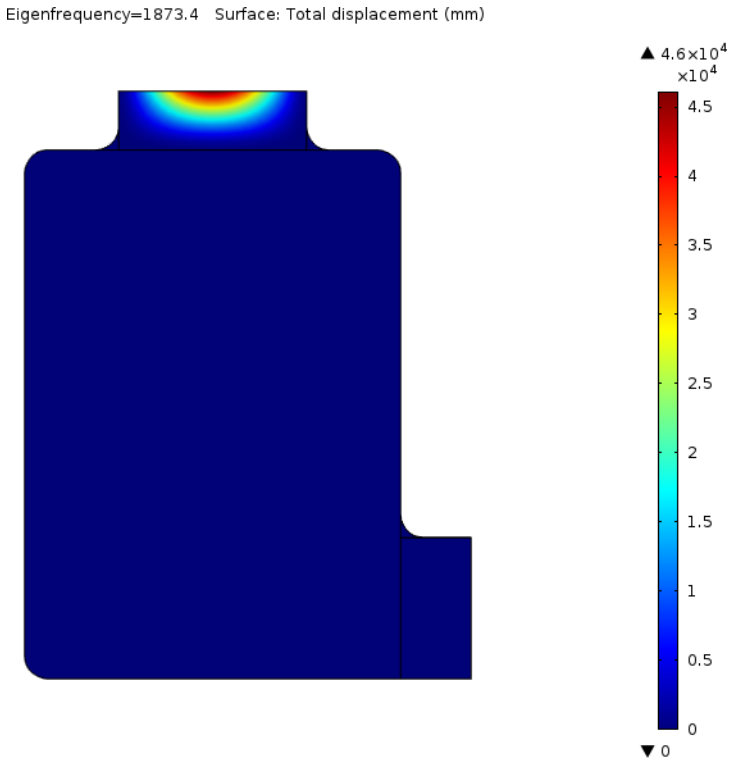

Fig. 30 (a). Surface Displacement (mm) for Eigen Frequency 1 = 1873 Hz

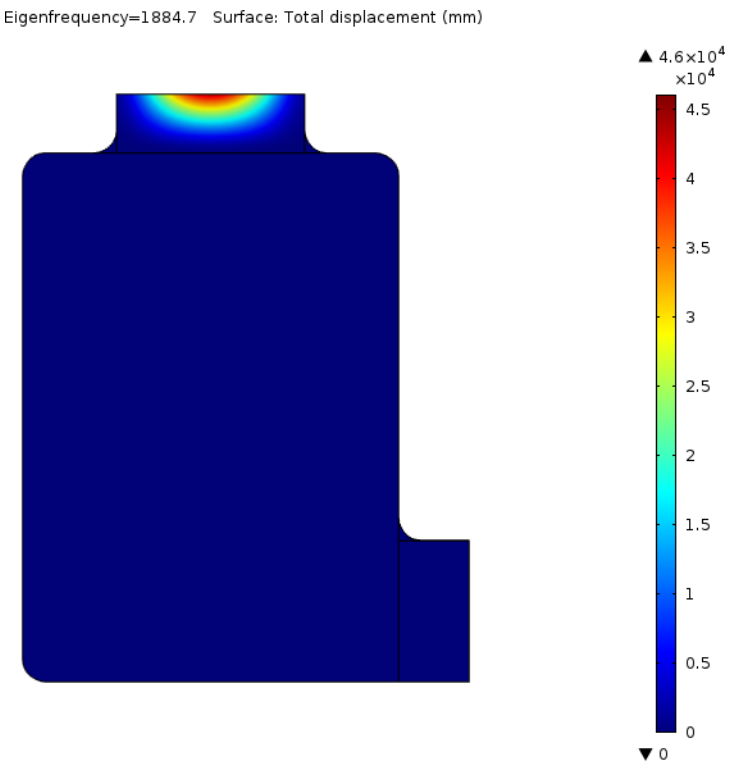

Fig. 30 (b). Surface Displacement (mm) for Eigen Frequency 2 = 1885 Hz.

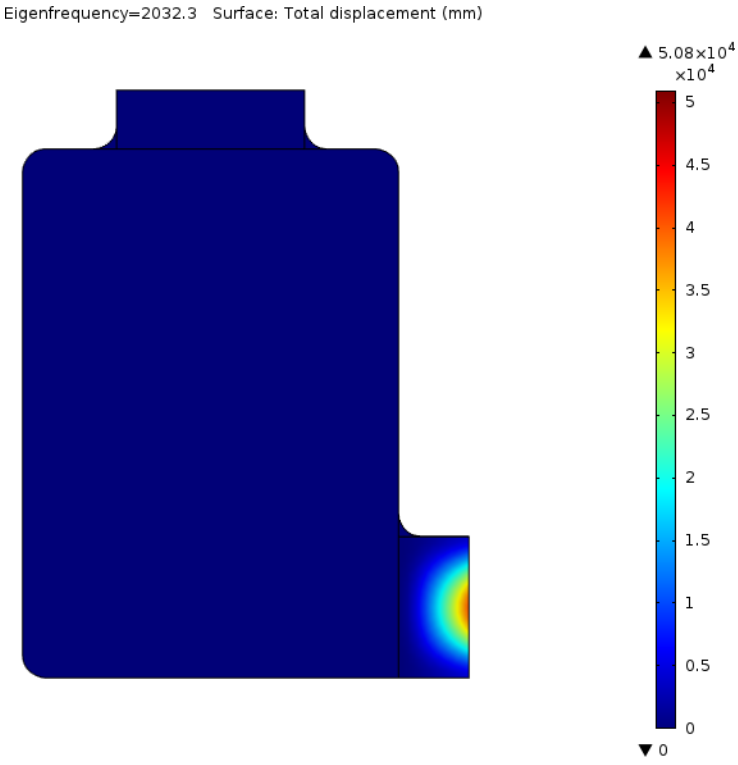

Fig. 30 (c). Surface Displacement (mm) for Eigen Frequency 3 = 2032 Hz

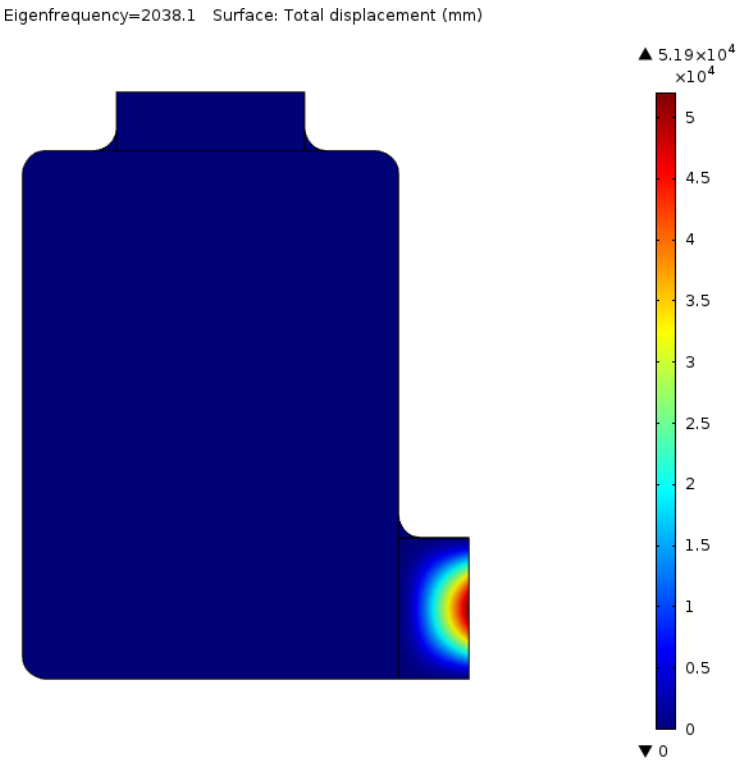

Fig. 30 (d). Surface Displacement (mm) for Eigen Frequency 4 = 2038 Hz

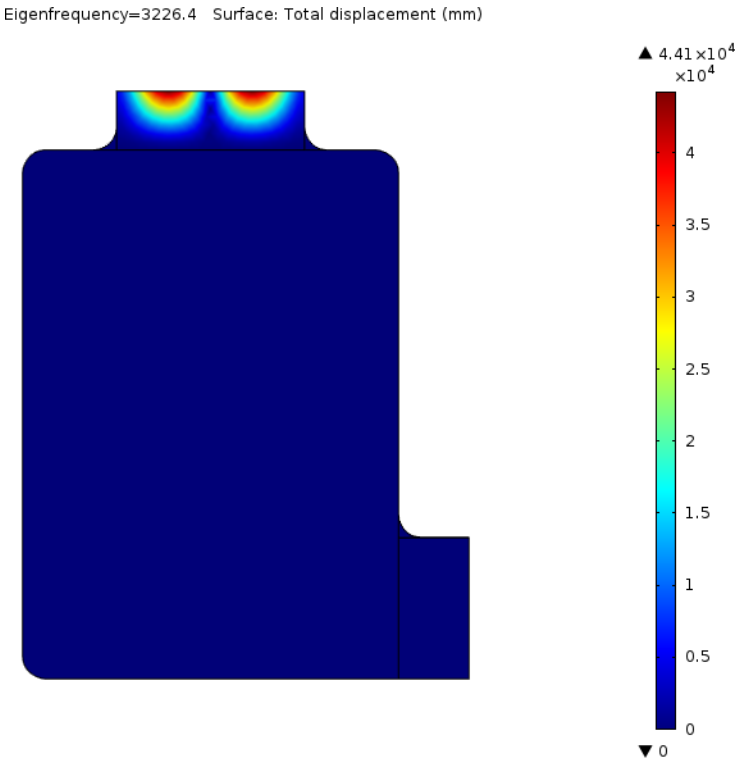

Fig. 30 (e). Surface Displacement (mm) for Eigen Frequency 5 = 3226 Hz

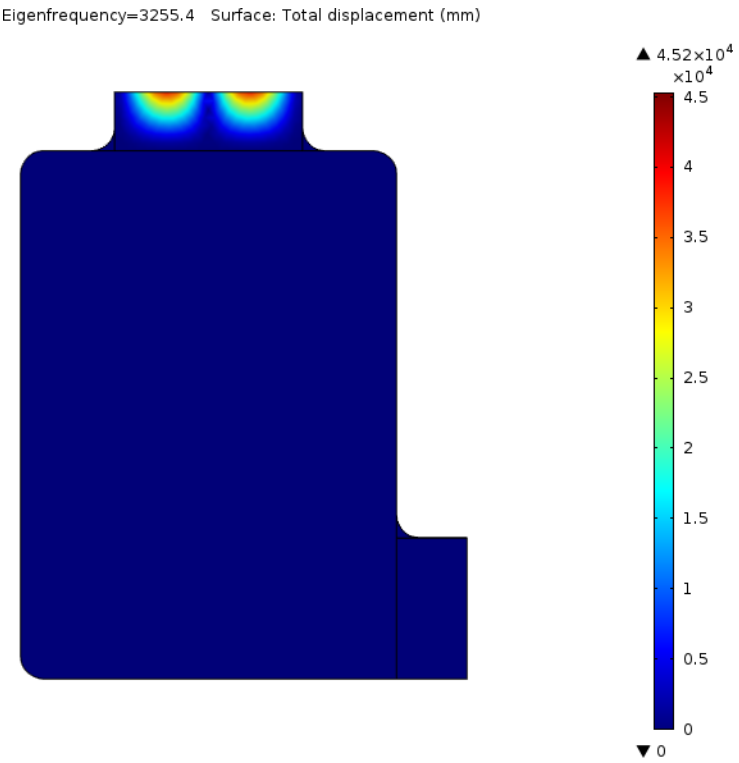

Fig 30 (f). Surface Displacement (mm) for Eigen Frequency 6 = 3255 Hz.

4.5 Manufacturing

After the studying the final design by varying different parameters such as diameter of pin and thickness of plate, the Design 3 with 1mm pin diameter and 1mm thickness of plate was selected as the best design. A structural and modal analysis was performed on the selected design to test the structural integrity before manufacturing. The plate was manufactured in two parts and welded together. The process selected for manufacturing was CNC machining due the intricate design. The below figures show plate after manufacturing.

Fig. 31 (a). Cooling plate – bottom

Fig. 31 (b). Cooling plate – top

CHAPTER 5

CONCLUSIONS AND FUTURE WORK

5.1 Conclusions

Lithium ion batteries are the power house of modern day electronic products. With their high energy and power density, the Li-ion batteries are becoming the most reliable option as a source of power for modes of transportation. With the advancements in electric vehicles and battery technology, the hybrid electric aircraft is the next step towards change. The possibility of powering electric motors and propulsion systems by Li-ion battery packs for heavy duty aircrafts is under study.

A Li-ion battery typically consists of cathode (positive charges electrode), an anode (negative charge electrode), a separator and an electrolyte packed inside a metal casing. The working principle of Li-ion battery is the conversion of chemical energy to electrical energy while heat is released as a byproduct of this energy conversion. The heat generated by a single cell can be dissipated into the atmosphere due to its low magnitude, but in hybrid and electric vehicles, numerous batteries are stacked together and the heat generated by the batteries is required to be removed from the system with an external agent or mechanism.

Thermal issues of Li-ion batteries affect the battery life, efficiency and overall safety of the battery pack. The efficiency and battery life cycle are affected by the increased operating temperatures. The rate degradation of the battery constituent components also increases at elevated temperatures. Thermal runaway is a disastrous phenomenon causing battery to decompose and generate excessive heat and poisonous gasses. Thermal runaway occurs in a time period of 10 seconds releasing massive amount of heat, hence increasing the surrounding temperatures.

Thermal management of Li-ion batteries implies to maintain the overall temperature of the battery pack to manufacture's specified operating range, dissipate excessive heat from the battery pack and increase the safety of the batteries. The optimal operating temperature as suggested by many studies for proper functioning of the battery and to improve the battery life cycle is between 22°C ~ 40 °C. Researchers and engineers around the world developed various methods and mechanisms to dissipate the heat generated by the Li-ion batteries. Studies showed the effect of temperatures on the battery life cycle and efficiency and also the causes and effect of thermal runaway. The focus of these studies was to attain maximum efficiency and cost-effectiveness without affecting the safety and reliability of the system. The studies were mostly developed around cylindrical batteries, as these are vastly used in the industry and very few on the large prismatic battery.

The aim of thesis was to develop a dual purpose cooling plate for prismatic Li-ion batteries which can dissipate heat during normal conditions and as well as during thermal runaway. For this, an experiment was designed to identify the trends and amount of local heat flux generated in the large prismatic battery. The battery was continuously charged

and discharged at a C-rate of 5C, for aggressive conditions. Heat flux sensors and thermocouples were used to measure the heat flux generated and temperatures across the surface of the battery. The results from this experiment were used as a baseline to design the cooling plates. The amount of heat generated during thermal runaway was also calculated.

Three designs of cooling plates namely Design 1, Design 2 and Design 3 were presented in this thesis with different geometric features. Each design is modelled upon the shortcoming of the previous designs. A numerical model of the cooling plates and battery was created in simulation software COMSOL. A combined heat transfer and laminar flow study was performed on all the cooling plate designs.

As the cooling plates are dual purpose, two sets of simulations were performed on the cooling plates (i.e.) Normal Operation with flow rate of 0.2 and 0.3 L/min and for Thermal Runaway with 20, 30, 40 L/min. The parameters under consideration for the selection of the best cooling plate design were:

- Ability to maintain the temperature below 25°C during Normal Operation.
- Ability to dissipate maximum heat during thermal runaway.
- Ability to maintain least pressure drop during both the operations.

From the results, during Normal Operation all the three designs were able to maintain the temperature below 25°C. During thermal runaway, Design 3 maintained the least temperature among all the other designs. The pressure drop for Design 3 was least as well for both the conditions. An optimization of Pin diameter and thickness of plates was

performed on Design 3. The analysis proved that Design 3 with 1mm diameter and 1mm thickness is the best option for the cooling plate.

At the end, this thesis proposed three designs of cooling plates and simulated them for two conditions and performed a comparative analysis of the three designs to select the best design which can maintain the temperature of the battery around 25°C as well as dissipate the heat generated during thermal runaway. A stress analysis and modal analysis was performed on the final design to test the structural integrity. The final design was manufactured.

5.2 Future works

For the continuation of this work:

- An experiment can be performed on the manufactured plate to examine its abilities as discussed in the thesis.
- The design can be made simpler for ease of manufacturing by adding slot to insert the top of the plate in the bottom.
- A combination of pin diameters can be simulated for better cooling capabilities.
- A complete battery thermal management with the designed cooling plates can be developed and tested.
- A control system which can detect thermal runaway can be designed to monitor the health of the Li-ion batteries in battery packs.

REFERENCES

[1] T. M. Bandhauer, S. Garimella, and T. F. Fuller, “A Critical Review of Thermal Issues in Lithium-Ion Batteries,” *J. Electrochem. Soc.*, vol. 158, no. 3, p. R1, 2011.

[2] D. H. Doughty and E. P. Roth, “A General Discussion of Li Ion Battery Safety,” *Interface Mag.*, vol. 21, no. 2, pp. 37–44, 2012.

[3] F. Leng, C. M. Tan, and M. Pecht, “Effect of Temperature on the Aging rate of Li Ion Battery Operating above Room Temperature,” *Sci. Rep.*, vol. 5, pp. 1–12, 2015.

[4] S. A. Khateeb, S. Amiruddin, M. Farid, J. R. Selman, and S. Al-Hallaj, “Thermal management of Li-ion battery with phase change material for electric scooters: Experimental validation,” *J. Power Sources*, vol. 142, no. 1–2, pp. 345–353, 2005.

[5] a a Pesaran, “<Battery thermal models for hybrid vehicle simulations.pdf>,” *J. Power Sources*, vol. 110, no. 2, pp. 377–382, 2002.

[6] V. Srinivasan and C. Y. Wang, “Analysis of Electrochemical and Thermal Behavior of Li-Ion Cells,” *J. Electrochem. Soc.*, vol. 150, no. 1, p. A98, 2003.

[7] K. Kumaresan, G. Sikha, and R. E. White, “Thermal Model for a Li-Ion Cell,” *J. Electrochem. Soc.*, vol. 155, no. 2, p. A164, 2008.

[8] X. Feng *et al.*, “Thermal runaway features of large format prismatic lithium ion battery using extended volume accelerating rate calorimetry,” *J. Power Sources*, vol. 255, pp. 294–301, 2014.

[9] T. G. Zavalis, M. Behm, and G. Lindbergh, “Investigation of Short-Circuit Scenarios in a Lithium-Ion Battery Cell,” *J. Electrochem. Soc.*, vol. 159, no. 6, p. A848, 2012.

[10] J. Xu, C. Lan, Y. Qiao, and Y. Ma, “Prevent thermal runaway of lithium-ion batteries with minichannel cooling,” *Appl. Therm. Eng.*, vol. 110, pp. 883–890, 2017.

[11] A. Nedjalkov *et al.*, “Toxic Gas Emissions from Damaged Lithium Ion Batteries—Analysis and Safety Enhancement Solution,” *Batteries*, vol. 2, no. 1, p. 5, 2016.

[12] M. Khan, M. Swierczynski, and S. Kær, “Towards an Ultimate Battery Thermal Management System: A Review,” *Batteries*, vol. 3, no. 1, p. 9, 2017.

[13] J. Neubauer and E. Wood, “Thru-life impacts of driver aggression, climate, cabin thermal management, and battery thermal management on battery electric vehicle utility,” *J. Power Sources*, vol. 259, pp. 262–275, 2014.

[14] T. Wang, K. J. Tseng, J. Zhao, and Z. Wei, “Thermal investigation of lithium-ion battery module with different cell arrangement structures and forced air-cooling strategies,” *Appl. Energy*, vol. 134, pp. 229–238, 2014.

[15] D. Chen, J. Jiang, G. H. Kim, C. Yang, and A. Pesaran, “Comparison of different cooling methods for lithium ion battery cells,” *Appl. Therm. Eng.*, vol. 94, pp. 846–854, 2016.

[16] F. He and L. Ma, “Thermal management of batteries employing active temperature control and reciprocating cooling flow,” *Int. J. Heat Mass Transf.*, vol. 83, pp.

164–172, 2015.

[17] X. M. Xu and R. He, “Research on the heat dissipation performance of battery pack based on forced air cooling,” *J. Power Sources*, vol. 240, pp. 33–41, 2013.

[18] M. R. Giuliano, A. K. Prasad, and S. G. Advani, “Experimental study of an air-cooled thermal management system for high capacity lithium-titanate batteries,” *J. Power Sources*, vol. 216, pp. 345–352, 2012.

[19] S. K. Mohammadian and Y. Zhang, “Thermal management optimization of an air-cooled Li-ion battery module using pin-fin heat sinks for hybrid electric vehicles,” *J. Power Sources*, vol. 273, pp. 431–439, 2015.

[20] S. Al-Hallaj, R. Kizilel, a. Lateef, R. Sabbah, M. Farid, and J. R. Selman, “Passive thermal management using phase change material (PCM) for EV and HEV Li- ion batteries,” *2005 IEEE Veh. Power Propuls. Conf.*, pp. 1–5, 2005.

[21] S. Al Hallaj and J. R. Selman, “A Novel Thermal Management System for Electric Vehicle Batteries Using Phase-Change Material,” *J. Electrochem. Soc.*, vol. 147, no. 9, p. 3231, 2000.

[22] Z. Wang, Z. Zhang, L. Jia, and L. Yang, “Paraffin and paraffin/aluminum foam composite phase change material heat storage experimental study based on thermal management of Li-ion battery,” *Appl. Therm. Eng.*, vol. 78, pp. 428–436, 2015.

[23] C. Lan, J. Xu, Y. Qiao, and Y. Ma, “Thermal management for high power lithium-ion battery by minichannel aluminum tubes,” *Appl. Therm. Eng.*, vol. 101, pp. 284–292, 2016.

[24] Q. Wang *et al.*, “Experimental investigation on EV battery cooling and heating by heat pipes,” *Appl. Therm. Eng.*, vol. 88, pp. 54–60, 2014.

[25] M. S. Wu, K. H. Liu, Y. Y. Wang, and C. C. Wan, “Heat dissipation design for lithium-ion batteries,” *J. Power Sources*, vol. 109, no. 1, pp. 160–166, 2002.

[26] G. Burban, V. Ayel, A. Alexandre, P. Lagonotte, Y. Bertin, and C. Romestant, “Experimental investigation of a pulsating heat pipe for hybrid vehicle applications,” *Appl. Therm. Eng.*, vol. 50, no. 1, pp. 94–103, 2013.

[27] A. Jarrett and I. Y. Kim, “Influence of operating conditions on the optimum design of electric vehicle battery cooling plates,” *J. Power Sources*, vol. 245, pp. 644–655, 2014.

[28] A. Jarrett and I. Y. Kim, “Design optimization of electric vehicle battery cooling plates for thermal performance,” *J. Power Sources*, vol. 196, no. 23, pp. 10359–10368, 2011.

[29] L. W. Jin, P. S. Lee, X. X. Kong, Y. Fan, and S. K. Chou, “Ultra-thin minichannel LCP for EV battery thermal management,” *Appl. Energy*, vol. 113, pp. 1786–1794, 2014.

[30] D. Haifeng, S. Zechang, W. Xuezhe, and Y. Shuqiang, “Design and Simulation of Liquid-cooling Plates for Thermal Management of EV Batteries,” *EVS28 Int. Electr. Veh. Symp. Exhib.*, pp. 1–7, 2015.

[31] M. M. Rahman, H. Y. Rahman, T. M. I. Mahlia, and J. L. Y. Sheng, “Liquid cooled plate heat exchanger for battery cooling of an electric vehicle (EV),” *IOP*

Conf. Ser. Earth Environ. Sci., vol. 32, no. 1, 2016.

[32] S. R. Hashemi, M. Montazeri, and M. Nasiri, “The compensation of actuator delay for hardware-in-the-loop simulation of a jet engine fuel control unit,” *Simulation*, vol. 90, no. 6, pp. 745–755, 2014.

[33] B. Rahmani and S. R. Hashemi, “Internet-based control of FCU hardware-in-the-loop simulators,” *Simul. Model. Pract. Theory*, vol. 56, pp. 69–81, 2015.

[34] A. Nazari and S. Farhad, “Heat generation in lithium-ion batteries with different nominal capacities and chemistries,” *Appl. Therm. Eng.*, vol. 125, pp. 1501–1517, 2017.

[35] E. Samadani, L. Gimenez, W. Scott, S. Farhad, M. Fowler, and R. Fraser, “Thermal Behavior of Two Commercial Li-Ion Batteries for Plug-in Hybrid Electric Vehicles.” SAE International , 2014.

[36] H. Y. Choi, J. S. Lee, Y. M. Kim, and H. Kim, “A Study on Mechanical Characteristics of Lithium-Polymer Pouch Cell Battery for Electrci Vehicle,” pp. 1–10, 2013.